

MOMENT-PRESERVING COMPUTATIONAL APPROACH FOR HIGH ENERGY CHARGED PARTICLE TRANSPORT

Third Interim Performance Report

**Anil K. Prinja
David A. Dixon**

**University of New Mexico
Chemical and Nuclear Engineering
Department MSC01 1120, 209 Farris
Engineering Center Albuquerque, NM 87131**

16 May 2014

Interim Report

APPROVED FOR PUBLIC RELEASE; DISTRIBUTION IS UNLIMITED.



**AIR FORCE RESEARCH LABORATORY
Space Vehicles Directorate
3550 Aberdeen Ave SE
AIR FORCE MATERIEL COMMAND
KIRTLAND AIR FORCE BASE, NM 87117-5776**

DTIC COPY

NOTICE AND SIGNATURE PAGE

Using Government drawings, specifications, or other data included in this document for any purpose other than Government procurement does not in any way obligate the U.S. Government. The fact that the Government formulated or supplied the drawings, specifications, or other data does not license the holder or any other person or corporation; or convey any rights or permission to manufacture, use, or sell any patented invention that may relate to them.

This report was cleared for public release by the 377 ABW Public Affairs Office and is available to the general public, including foreign nationals. Copies may be obtained from the Defense Technical Information Center (DTIC) (<http://www.dtic.mil>).

AFRL-RV-PS-TR-2014-0139 HAS BEEN REVIEWED AND IS APPROVED FOR PUBLICATION IN ACCORDANCE WITH ASSIGNED DISTRIBUTION STATEMENT.

//SIGNED//

Adrian Wheelock
Project Manager, AFRL/RVBXR

//SIGNED//

Glenn M. Vaughan, Colonel, USAF
Chief, Battlespace Environment Division

This report is published in the interest of scientific and technical information exchange, and its publication does not constitute the Government's approval or disapproval of its ideas or findings.

REPORT DOCUMENTATION PAGE				Form Approved OMB No. 0704-0188	
Public reporting burden for this collection of information is estimated to average 1 hour per response, including the time for reviewing instructions, searching existing data sources, gathering and maintaining the data needed, and completing and reviewing this collection of information. Send comments regarding this burden estimate or any other aspect of this collection of information, including suggestions for reducing this burden to Department of Defense, Washington Headquarters Services, Directorate for Information Operations and Reports (0704-0188), 1215 Jefferson Davis Highway, Suite 1204, Arlington, VA 22202-4302. Respondents should be aware that notwithstanding any other provision of law, no person shall be subject to any penalty for failing to comply with a collection of information if it does not display a currently valid OMB control number. PLEASE DO NOT RETURN YOUR FORM TO THE ABOVE ADDRESS.					
1. REPORT DATE (DD-MM-YYYY) 16-05-2014		2. REPORT TYPE Interim Report		3. DATES COVERED (From - To) 01 May 2013 to 01 May 2014	
4. TITLE AND SUBTITLE MOMENT-PRESERVING COMPUTATIONAL APPROACH FOR HIGH ENERGY CHARGED PARTICLE TRANSPORT Second Interim Performance Report				5a. CONTRACT NUMBER FA9453-11-1-0276	
				5b. GRANT NUMBER	
				5c. PROGRAM ELEMENT NUMBER 62601F	
6. AUTHOR(S) Anil K. Prinja and David A. Dixon				5d. PROJECT NUMBER 1010	
				5e. TASK NUMBER PPM00011354	
				5f. WORK UNIT NUMBER EF004076	
7. PERFORMING ORGANIZATION NAME(S) AND ADDRESS(ES) University of New Mexico Chemical and Nuclear Engineering Department MSC01 1120, 209 Farris Engineering Center Albuquerque, NM 87131				8. PERFORMING ORGANIZATION REPORT NUMBER	
9. SPONSORING / MONITORING AGENCY NAME(S) AND ADDRESS(ES) Air Force Research Laboratory Space Vehicles Directorate 3550 Aberdeen Avenue SE Kirtland AFB, NM 87117-5776				10. SPONSOR/MONITOR'S ACRONYM(S) AFRL/RVBXR	
				11. SPONSOR/MONITOR'S REPORT NUMBER(S) AFRL-RV-PS-TR-2014-0139	
12. DISTRIBUTION / AVAILABILITY STATEMENT Approved for public release; distribution is unlimited. (377ABW-2014-0537 dtd 10 Jul 2014)					
13. SUPPLEMENTARY NOTES					
14. ABSTRACT An algorithm for generating Generalized Boltzmann Fokker-Plank (GBFP) discrete cross-section data and the implementation of the discrete and hybrid models in Geant4 are described. A test suite with various problems of interest was completed and many of the results from the test suite are presented. Several tools for tallying quantities of interest required for the test suite were incorporated. New analog and GBFP models that utilize elastic DCS data were implemented and testing of the implementation is currently in progress.					
15. SUBJECT TERMS Reduced Physics Models, Geant4, CEASE					
16. SECURITY CLASSIFICATION OF:			17. LIMITATION OF ABSTRACT	18. NUMBER OF PAGES	19a. NAME OF RESPONSIBLE PERSON
a. REPORT Unclassified	b. ABSTRACT Unclassified	c. THIS PAGE Unclassified			Adrian Wheelock
			Unlimited	54	19b. TELEPHONE NUMBER (include area code)

This page is intentionally left blank.

Table of Contents

1. INTRODUCTION	1
2. BACKGROUND	1
3. METHODS, PROCEDURES, and ASSUMPTIONS.....	7
3.1. Quadrature Methods.....	7
3.2. GBFP Discrete Cross-section Generation.....	9
3.3. GBFP Hybrid Cross-Section Generation	13
3.4. Implementation of the GBFP Models in Geant4 Test Code	16
4. RESULTS AND DISCUSSION	18
4.1. CEASE-like Problem	21
4.2. Angular Deflection Distributions.....	24
4.3. Energy-Loss Spectra	31
4.4. Dose-Depth Curves	33
4.5. Two-Dimension Dose Deposition.....	36
4.6. Reflection and Transmission Fractions.....	39
5. CONCLUSIONS	42
REFERENCES	43
LIST OF SYMBOLS, ABBREVIATIONS, AND ACRONYMS	44

List of Figures

Figure 1: One-Dimension Slab Problem Schematic.	19
Figure 2: CEASE Particle Telescope Schematic.	21
Figure 3: Reflected Energy Spectrum (a) and Relative Difference (b) for Electron Pencil Beam With Power Law Energy Distribution in 150 Microns of Silicon.	22
Figure 4: Dose (a) and Relative Difference (b) for Electron Pencil Beam With Power Law Energy Distribution in 150 Microns of Silicon.	22
Figure 5: Dose (a) and Relative Difference (b) for Electron Pencil Beam With Power Law Energy Distribution in 500 Microns of Silicon.	23
Figure 6: Transmitted Angular Distributions for 100-keV and 10000-keV Electrons in Silicon, Copper, and Gold Slabs with Thickness of One Step.	25
Figure 7: Comparison of GBFP and Benchmark Transmitted Angular Distributions using (a) Discrete and (c) Hybrid and the Relative Differences for (b) Discrete and (d) Hybrid for 100-keV Electrons in Silicon.	26
Figure 8: Comparison of GBFP and Benchmark Transmitted Angular Distributions using (a) Discrete and (c) Hybrid and the Relative Differences for (b) Discrete and (d) Hybrid for 10000-keV Electrons in Silicon.	27
Figure 9: Reflected Angular Distributions for 100-keV and 10000-keV Electrons in Silicon, Copper, and Gold Slabs with a Thickness of One Step.	28
Figure 10: Comparison of GBFP and Benchmark Reflected Angular Distributions using (a) Discrete and (c) Hybrid and the Relative Differences for (b) Discrete and (d) Hybrid for 100-keV Electrons in Silicon.	29
Figure 11: Comparison of GBFP and Benchmark Reflected Angular Distributions using (a) Discrete and (c) Hybrid and the Relative Differences for (b) Discrete and (d) Hybrid for 10000-keV Electrons in Silicon.	30
Figure 12: Reflected Energy-Loss Spectra (a) and Relative Difference (b) for 100-keV Electrons in Gold.	31
Figure 13: Transmitted Energy-Loss Spectra (a) and Relative Difference (b) for 100-keV Electrons in Gold.	32
Figure 14: Transmitted Energy-Loss Spectra (a) and Relative Difference (b) for 10000-keV Electrons in Gold.	32

Figure 15: Analog Dose Profile for 100-keV Electrons in Gold Slab with a Thickness of One Step.	33
Figure 16: Analog Dose Profile for 10000-keV Electrons in Gold Slab with a Thickness of One Step.....	34
Figure 17: Dose Profiles (a) and Relative Difference (b) for 100-keV Electrons in Gold.	34
Figure 18: Dose Profiles (a) and Relative Difference (b) for 10000-keV Electrons in Gold. ..	35
Figure 19: Two-Dimension Dose Deposition Problem Schematic.	36
Figure 20: Dose Deposition Benchmark for 250-keV Electrons in Silicon Cube Gold with Insert.	36
Figure 21: Dose Deposition for 250-keV Electrons in Silicon Cube With Gold Insert Using (A) GBFP 1 Discrete Angle, 1 Discrete Energy, (b) Geant4 Default Physics with 0.04 range Factor, (c) GBFP 8 Discrete Angles, 1 Discrete Energy, and (d) Geant4 Default Physics with 0.004 range factor.	37
Figure 22: The Fraction of Particles Reflected (a) and the relative difference for (b) Single-Angle, Single-Energy DCS, (c) Single-Angle, Analog Inelastic DCS, and (d) Four-Angle, Analog Inelastic DCS.....	40
Figure 23: The Fraction of Particles Transmitted (a) and the relative difference for (b) Single-Angle, Single-Energy DCS, (c) Single-Angle, Analog Inelastic DCS, and (d) Four-Angle, Analog Inelastic DCS.....	41

List of Tables

Table 1: Moments of the Screened Rutherford Analog DCS	10
Table 2: Non-classical Recurrence Coefficients for Example Problem	11
Table 3: Example Discrete Cross-Section Before Regularizing	11
Table 4: Example Discrete Cross-Section After Regularizing.....	11
Table 5: Ratio of Wall Time for Analog Simulation to Wall Time for GBFP Simulation.....	19
Table 6: Ratio of Wall Time for Analog Simulation to Wall Time for GBFP Simulation	
Continued.....	20

1. INTRODUCTION

The following sections present work completed under the UNM/AFRL research grant FA9453-11-1-0276 since May 2013. During this time period, the Generalized Boltzmann Fokker-Plank (GBFP) advanced physics models were expanded to include both discrete and hybrid differential cross section (DCS) models. In addition, the analog models that are the basis of the GBFP physics were expanded to include the following DCSs: the screened Rutherford elastic scattering DCS, the partial wave expansion elastic scattering DCS, the Rutherford inelastic DCS, and the Möller inelastic DCS. Tools for tallying quantities like dose, charge deposition, transmission and reflection, angular distributions, energy spectra, and lateral and longitudinal distributions were implemented and tested. Finally, a test suite including a wide variety of problems was completed. The remainder of the paper will cover background material, discuss the methods utilized, and present results obtained from the test suite.

2. BACKGROUND

Solution to the Boltzmann transport equation for electrons requires information about the interactions that an electron can undergo. This information is captured by the DCSs and describes the probability that a particle will scatter through some angle or lose some energy to the medium. In addition, the total cross section is obtained from the DCS and characterizes the length scale of the physics. For electrons, the mean free path (MFP) or the inverse of the total cross section is extremely small, so particles suffer thousands of collisions while slowing down. Also, the DCSs are peaked about small changes in the state of the electron. As a result, analog Monte Carlo is extremely computationally inefficient for electrons above a few hundred keV.

Approximate methods were developed to alleviate the computational effort required for analog Monte Carlo simulation of electrons. However, methods like condensed history (CH) introduce error on the order of the fixed distance traveled by the electron between collisions or the step and CH requires special boundary crossing algorithms to mitigate additional error incurred at material interfaces. The GBFP method is an approximate method, but unlike CH, the GBFP method is a single-event Monte Carlo method. That is, the distance between collisions or the step is exponentially distributed, so no boundary crossing algorithms are required. In addition, the GBFP method introduces moment-preserving, approximate DCSs with systematically controllable accuracy by preservation of more moments.

Like analog Monte Carlo, the GBFP physics models require a total cross section and a DCS for each interaction simulated. The cross sections are used to sample distance to collision, scattering angle, and energy-loss. Not only are the approximate DCSs critical to the GBFP method, but also the analog DCSs are required to construct the approximate DCSs using moments of the analog DCSs. Therefore, some attention is given to the DCSs currently implemented.

The predominant interactions that are considered in this work are elastic scattering with target nuclei and inelastic scattering with orbital electrons. Elastic scattering is a Coulombic interaction between primary electrons and target nuclei that can result in a change in the primary electron's direction (energy loss due to elastic scattering is negligible). Inelastic scattering is a Coulombic interaction between the primary electrons and the atomic electrons where energy from the

primary electrons is transferred to the atomic electrons (change in direction due to inelastic scattering of the primary electrons is neglected). Currently, elastic scattering models implemented include the screened Rutherford DCS [1] and the partial-wave expansion DCS [2]. The screened Rutherford DCS is a widely applicable, but simplified model. The benefit of using the screened Rutherford cross section is that it is in a continuous form or

$$\Sigma_s(\vec{r}, E, \mu_0) = \frac{C(E)}{[1 - \mu_0 + 2\eta(E)]^2}, \quad (2.1)$$

where $\mu_0 = \cos(\theta_0)$ is the deflection cosine, $\eta(E)$ is the screening parameter, and $C(E)$ is the material constant. The screening parameter is given by

$$\eta(E) = \frac{\frac{Z^{2/3}}{4} \left[1.13 + 3.76 \left(\frac{Z}{137} \right)^2 (T+1)^2 T^{-1} (T+2)^{-1} \right]}{(0.885 \cdot 137)^2 T(T+2)}, \quad (2.2)$$

where Z is the atomic number of the target nucleus and $T = E / m_0 c^2$ is the particle energy per rest mass energy. For electrons, $m_0 c^2 = 0.510998910 \text{ MeV}$. The material constant is given by

$$C(E) = \frac{2\pi r_0^2 \rho N_A Z(Z+1)}{A} \frac{(T+1)^2}{T^2 (T+2)^2}, \quad (2.3)$$

where A is the atomic mass, $r_0 = 2.8179403267 \times 10^{-13} \text{ cm}$ is the classical electron radius, ρ is the material density, and N_A is Avogadro's number. In contrast to the screened Rutherford DCS, the partial-wave DCSs are given by

$$\Sigma_n(\mu) = |f(\mu)|^2 + |g(\mu)|^2, \quad (2.4)$$

where

$$f(\mu) = \frac{1}{2ik} \sum_{l=0}^{\infty} \{ (l+1) [\exp(2i\delta_{l,1}) - 1] + l [\exp(2i\delta_{l-1}) - 1] \} P_l(\mu) \quad (2.5)$$

and

$$g(\mu) = \frac{1}{2ik} \sum_{l=0}^{\infty} [\exp(2i\delta_{l,1}) - \exp(2i\delta_{l-1})] P_l^1(\mu). \quad (2.6)$$

It is beyond the scope of this report to discuss the process of calculating the partial-wave DCS (see ELSEPA [2]); however, it is important to note that there is no analytical form of eq. 2.4. Therefore, computer codes are used to generate partial-wave DCS libraries. The motivation for

using the partial-wave DCS is because it is the most accurate representation of elastic scattering currently available. It also provides an additional application to demonstrate the effectiveness and flexibility of the GBFP method. That is, the GBFP method does not depend on the form of the DCS, rather the moments. Therefore, DCSs can be continuous or discrete so long as moments of the DCS can be accurately calculated.

There are two analog inelastic scattering models currently implemented in the Geant4 [4] test code. The inelastic DCS models currently implemented includes the Rutherford DCS [3] given by

$$\Sigma_e(E, Q) = \frac{K(E)}{Q^2}, \quad (2.7)$$

where the material constant, $K(E)$, is

$$K(E) = \frac{2\pi r_0^2 \rho N_A Z}{A\beta^2}, \quad (2.8)$$

$\beta = v/c$, is the particle velocity per c (c being the speed of light), and Q is the energy transferred from the incident particle to the atomic electron. The more accurate Möller [3] DCS was also implemented and is given by

$$\Sigma_e(E, Q) = K(E) \left[\frac{1}{Q^2} + \frac{1}{(E-Q)^2} + \frac{1}{(E+m_0c^2)^2} - \frac{m_0c^2(2E+m_0c^2)}{Q(E-Q)(E+m_0c^2)^2} \right]. \quad (2.9)$$

Given the aforementioned DCS models, the goal of the Monte Carlo method is to solve the Boltzmann transport equation for the selected physics by simulating the particle behavior according the DCSs. For example, the Boltzmann transport equation for electrons that can undergo the interactions detailed above is

$$\vec{\Omega} \cdot \nabla \psi(E, \vec{\Omega}) + \Sigma_t(E) \psi(E, \vec{\Omega}) = \int_{4\pi} d\Omega' \Sigma_n(E, \vec{\Omega}' \cdot \vec{\Omega}) \psi(E, \vec{\Omega}') + \int_0^\infty dE' \Sigma_e(E' \rightarrow E) \psi(E', \vec{\Omega}). \quad (2.10)$$

In the eq. 2.10 the spatial dependence is implied for compactness, but in the following definitions the spatial dependence is explicit:

- $\psi(\vec{r}, E, \vec{\Omega})$ Angular flux
- $\Sigma_n(\vec{r}, E, \mu_0)$ Macroscopic elastic scattering cross section
- $\Sigma_e(\vec{r}, E, Q)$ Macroscopic inelastic scattering cross section
- $\Sigma_t(\vec{r}, E)$ Total macroscopic interaction cross section

where \vec{r} is position vector, E is the particle energy, and $\vec{\Omega}$ the direction of the particle. The prime notation on E and $\vec{\Omega}$ corresponds to the particles energy or direction before a collision

occurs. The left-hand side of eq. 2.10 corresponds to particles leaving the phase space or particle losses and the right-hand side corresponds to particles entering the phase space or particle gains. The first loss term,

$$\vec{\Omega} \cdot \nabla \psi(\vec{r}, E, \vec{\Omega}) \equiv \text{Leakage},$$

accounts for particles leaking or leaving the differential volume. The second loss term

$$\Sigma_t(E) \psi(\vec{r}, E, \vec{\Omega}) \equiv \text{Outscatter},$$

accounts for outscatter or particles leaving the energy or angular space by changing direction or energy. The first gain term,

$$\int_{4\pi} d\Omega' \Sigma_n(E, \vec{\Omega}' \cdot \vec{\Omega}) \psi(E, \vec{\Omega}') \equiv \text{Elastic Inscatter},$$

accounts for particles scattering into the angular phase space. The second gain term,

$$\int_0^\infty dE' \Sigma_e(E' \rightarrow E) \psi(E', \vec{\Omega}) \equiv \text{Inelastic Inscatter},$$

accounts for particles scattering into the energy phase space. According to eq. 2.10 and a corresponding boundary condition or fixed source, a source particle is created with a position, energy, and direction. Next, the particle streams or moves a distance to a collision site. This process is sampled according to the following probability distribution function

$$P(s)ds = \Sigma_t \exp(-\Sigma_t s) ds, \quad (2.11)$$

where s is the distance to collision. Given a distance to collision, the particle is moved to a collision site. At the collision site, the collision type is randomly sampled according to the probability of the respective collision type. The probability of an elastic scatter is the ratio of the total elastic scatter cross section, $\Sigma_{n,0}$, to the total interaction cross section, $\Sigma_t = \Sigma_{n,0} + \Sigma_{e,0}$, or

$$P_n = \frac{\Sigma_{n,0}}{\Sigma_t}, \quad (2.12)$$

and the probability of an inelastic scatter is the ratio of the total inelastic scatter cross section, $\Sigma_{e,0}$, to the total interaction cross section, Σ_t , or

$$P_e = \frac{\Sigma_{e,0}}{\Sigma_t}. \quad (2.13)$$

Given the collision type, the collision outcome is determined by sampling the corresponding DCS. This is accomplished by direct or rejection sampling techniques. For example, the screened Rutherford elastic scattering DCS is invertible, so a direct technique is used or

$$\mu_0 = 1 - \frac{2\eta\xi}{1 - \xi + \eta}. \quad (2.14)$$

where ξ is a random number sampled uniformly between zero and one. However, the Möller DCS is not invertible so a rejection technique must be used. Rejection techniques are well documented for the Möller DCS (see Geant4 Physics Reference Manual [5]) and not summarized here because it is an involved process. Regardless of the technique, the outcome is the same. That is, an energy loss is sampled according to the physics governing the collision type or the DCS. This process of sampling distance to collision, collision type, and collision outcome is repeated for each source particle until all source particles are complete. During the simulation process, tallies of interest are accumulated. As previously mentioned, we are interested in quantities like dose, charge deposition, transmission and reflection, angular distributions, energy spectra, and lateral and longitudinal distributions. To tally the various quantities of interest, a running sum is accumulated as the particles transverse the medium. For example, in a one-dimensional slab, dose in $\frac{\text{MeV} \cdot \text{cm}^2}{g}$ per source particle in the i^{th} cell is

$$D_i = \frac{1}{N\rho\Delta x_i} \sum_j d_{i,j}, \quad (2.15)$$

where $d_{i,j}$ is the dose deposited in the i^{th} cell by the j^{th} source particle, Δx_i is the width of the i^{th} cell, and N is the total number of source particles.

This simple description of the Monte Carlo algorithm is valid for analog or single-event Monte Carlo where collision sites are exponentially distributed. One significant difference between the GBFP method and other approximations is that the GBFP method is a single-event method. Therefore, pre-existing single-event Monte Carlo algorithms can be used, so no code modifications are necessary to use this approximation. That is because the GBFP method simply relies on approximate DCSs. There is a very subtle difference between the transport equation solved using the GBFP method and the analog transport equation in eq. 2.10. After substituting the approximate cross sections the transport equation becomes

$$\bar{\Omega} \cdot \nabla \psi(E, \bar{\Omega}) + \tilde{\Sigma}_t(E) \psi(E, \bar{\Omega}) = \int_{4\pi} d\Omega' \tilde{\Sigma}_n(E, \bar{\Omega}' \cdot \bar{\Omega}) \psi(E, \bar{\Omega}') + \int_0^\infty dE' \tilde{\Sigma}_e(E' \rightarrow E) \psi(E', \bar{\Omega}). \quad (2.16)$$

where $\tilde{\Sigma}$ implies that the cross section is approximate. Notice that the form of operators in eq. 2.10 and eq. 2.16 are the same. For this reason, many of the issues encountered when using CH methods, like boundary crossings and step-length limitations, are avoided when using the GBFP method. Unlike CH, the transport equation remains unchanged. The only question that remains is how does one construct a GBFP DCS such that a solution eq. 2.16 is a good approximation of the analog solution.

To do so, Lewis theory [6] is utilized. Lewis theory provides a relationship between Legendre moments of the elastic scattering DCS and space-angle moments of the solution. That is, if an approximate DCS preserves a finite number of Legendre moments, L , of the analog DCS, then it is possible to preserve $p+q=L$ space-angle moments of the analog solution, where

$$M_l = 2\pi \int_{-1}^1 P_l(\mu) \Sigma_n(E, \mu) d\mu, \quad (2.17)$$

are the Legendre moments of the analog elastic scattering DCS. The space-angle moments of the solution are

$$\varphi_{p,q} = \int_{-\infty}^{+\infty} dz \int_{-1}^1 z^p \mu^q \Sigma_n(E, \mu) d\mu. \quad (2.18)$$

Lewis theory is only valid in an infinite medium, but it does emphasize the relationship between moments of the DCS and moments of the solution. Therefore, the GBFP DCSs are constructed such that they preserve moments of the analog DCSs. To do so, we write down a system of equations,

$$M_l = \tilde{M}_l, \quad l=1, 2, \dots, L \quad (2.19)$$

where

$$\tilde{M}_l = 2\pi \int_{-1}^1 P_l(\mu) \tilde{\Sigma}_n(E, \mu) d\mu. \quad (2.20)$$

In eq. 2.19, L is determined by the number of unknown parameters used to construct the GBFP DCS. For both the discrete DCS and the hybrid DCS, there are a total of $2N$ points and weights that must be determined. Thus, $L=2N$ for the system in eq. 2.19. As an example, we take a discrete DCS with the following form

$$\tilde{\Sigma}_n(E, \mu) = \sum_{n=1}^N \frac{\alpha_n(E)}{2\pi} \delta[\mu - \zeta_n], \quad (2.21)$$

where ζ_n are the discrete points and α_n are the corresponding weights. Substituting eq. 2.21 into eq. 2.19 gives

$$M_l = \alpha_1(E)P_l(\zeta_1) + \dots + \alpha_N(E)P_l(\zeta_N), \quad l=1, 2, \dots, 2N. \quad (2.22)$$

We now have a system of $2N$ points and weights that we can solve such that the first moment and higher order moments of the discrete DCS are equivalent to the moments of the analog DCS. Therefore, the zeroth moment or the total cross section is not preserved. The result is a smoother cross section with a longer mean free path (MFP), which are both features of the analog DCS that result in substantial computational cost for analog Monte Carlo simulations. A smoother

DCS with a longer MFP that preserves moments of the analog DCS is the key to accurately and efficiently approximating eq. 2.10.

The goal of the GBFP method is to utilize approximate DCSs that are smoother and have longer MFPs. However, there is a certain level of detail that is required to obtain these ideal DCSs. The following section provides a thorough discussion of the process of obtaining various GBFP DCSs.

3. METHODS, PROCEDURES, AND ASSUMPTIONS

The current implementation of the GBFP method allows for two approximate DCSs: discrete and hybrid DCS models. The discrete DCS is a set of discrete points and weights. Whereas, the hybrid DCS is a combination of a smooth tail and a discrete peak. Both DCSs require calculation of discrete points and weights, so the following sections discuss the general methods used to generate the DCSs and the details specific to the discrete and hybrid DCSs. In addition, Geant4 implementation details relevant to the work completed to date are presented.

3.1. Quadrature Methods

In section 2, the system of equations in eq. 2.21 demonstrates the GBFP concept, but that system is not directly invertible due to numerical instabilities. Therefore, we turn to a method typically used to generate quadrature sets as an alternative approach. The aim of Gaussian quadrature is to obtain the points, (x_1, x_2, \dots, x_N) , and weights, (w_1, w_2, \dots, w_N) , such that

$$\int_a^b w(\mu) f(\mu) d\mu = \sum_{i=1}^N w_i f(x_i) \quad (3.1)$$

is equivalent for polynomials, $f(\mu)$, of order $2N-1$ and less. To obtain the points and weights one must generate N polynomials that are orthogonal with respect to the weight function, $w(\mu)$. The polynomials are then used to obtain the points and weights. That is, the zeros of the order N polynomial are the points and the weights are given by

$$w_i = \frac{\langle p_{N-1} | p_{N-1} \rangle}{p_{N-1}(x_i) p'_{N-1}(x_i)}. \quad (3.2)$$

To generate orthogonal polynomials, the recurrence coefficients, (α_j, β_j) , satisfying

$$p_{j+1}(x) = (x - \alpha_j) p_j(x) - \beta_j p_{j-1}(x) \quad (3.3)$$

are required. In the context of this discussion, there are two types of orthogonal polynomials, classical and non-classical. Classical polynomials are orthogonal with respect to classical weight functions (examples include Legendre, Jacobi, Chebyshev, Laguerre, Hermite, and so on). There are typically well-known recurrences and recurrence coefficients for classical orthogonal

polynomials. That is, computation of the recurrence coefficients is unnecessary, so generating Gauss-Legendre quadrature, Gauss-Jacobi quadrature, and so forth is just a matter of determining the points and weights from the known recurrence coefficients. However, it can be advantageous to generate quadrature sets corresponding to non-classical weight functions. Therefore, an additional step is required where the recurrence coefficients are obtained for the polynomials that are orthogonal with respect to the non-classical weight function.

It is possible to obtain the recurrence coefficients for non-classical orthogonal polynomials using the modified Chebyshev Algorithm (MCA). The MCA is derived by Gautschi [7] and is a mapping procedure for mapping the recurrence coefficients of classical orthogonal polynomials to the recurrence coefficients non-classical orthogonal polynomials with modified moments given by

$$\nu_j = \int_a^b \pi_j(x) w(x) dx, \quad (3.4)$$

where $\pi_j(x)$ is a classical orthogonal polynomial of order j . Given the modified moments and the recurrence coefficients of classical orthogonal polynomials, the MCA returns the recurrence coefficients of non-classical orthogonal polynomials that are used to generate the corresponding quadrature set. The MCA is typically used when integrating specialized functions that cannot be factored into a classical weight function and a polynomial. However, the system encountered when generating a GBFP DCS can be recast into a Gaussian quadrature problem for a non-classical weight function.

Before moving to the details of applying the MCA to the GBFP method, we will write down the final step in generating the points and weights. There are a number of methods for obtaining the discrete points and weights, but the method used in this work is due to Golub and Welsch [8]. Wilf recognized that the Gaussian quadrature system could be written in terms of an eigenvalue problem. The important result is that the zeros of the order N polynomial are equivalent to the eigenvalues of the Jacobi matrix

$$J = \begin{pmatrix} \alpha_0 & \sqrt{\beta_1} & 0 & \cdots & & 0 \\ \sqrt{\beta_1} & \alpha_1 & \sqrt{\beta_2} & & & \vdots \\ 0 & \sqrt{\beta_2} & \alpha_2 & \sqrt{\beta_3} & & \\ \vdots & & \sqrt{\beta_3} & \alpha_3 & \ddots & 0 \\ & & & \ddots & \ddots & \sqrt{\beta_{N-1}} \\ 0 & \cdots & & 0 & \sqrt{\beta_{N-1}} & \alpha_N \end{pmatrix}, \quad (3.5)$$

where (α_j, β_j) are the recurrence coefficients of the orthogonal polynomials (classical or non-classical). The first entry of the i^{th} eigenvector, \tilde{q}_i , squared corresponds to the i^{th} weight or

$$w_i = q_{i1}^2. \quad (3.6)$$

Finally, it is important to note that the GBFP method requires Gauss-Radua quadrature where one of the points is constrained to be the upper or lower bound of the integral in eq. 3.1. Given this constraint, the process of obtaining the correct Jacobi matrix is outlined by Golub [9]. The important results are summarized below. We wish to determine a polynomial such that $p_{N+1}(a) = 0$ or $p_{N+1}(b) = 0$, where a and b are the limits of the integral in 3.1. This implies that

$$\alpha_{N+1} = a - \beta_N \frac{p_{N-1}(a)}{p_N(a)} \quad (3.7)$$

or

$$\alpha_{N+1} = b - \beta_N \frac{p_{N-1}(b)}{p_N(b)}. \quad (3.8)$$

Now, the Jacobi matrix is expanded from an N^2 to an $(N+1)^2$ matrix with the constraint that one of the points, \mathbf{x}_i , is a or b . Given a method for obtaining discrete points and weights corresponding to a non-classical weight function, it is possible to recast the GBFP cross section construction problem into a similar quadrature problem of a non-classical weight function.

3.2. GBFP Discrete Cross-section Generation

We can rewrite eq. 3.1 in the following form:

$$\int_{-1}^1 \Sigma_n(E, \mu) f(\mu) d\mu = \sum_{n=1}^N \alpha_n(E) f(\zeta_n). \quad (3.9)$$

We would like to satisfy this equation for polynomials of order $2N-1$ or less. Specifically, we would like to satisfy the above equation for $f(\mu) = P_l(\mu)$, where $P_l(\mu)$ is a Legendre polynomial. Since eq. 3.9 holds for all polynomials, the same will be true if $f(\mu) = P_l(\mu)$ or

$$\int_{-1}^1 \Sigma_n(E, \mu) P_l(\mu) d\mu = \sum_{n=1}^N \alpha_n(E) P_l(\zeta_n). \quad (3.10)$$

Given the discussion in the previous section, it should be clear that eq. 3.9 and 3.10 can be satisfied and the process of mapping the known recurrence coefficients to those of non-classical recurrence coefficients using the MCA is a viable approach. These particular non-classical recurrence coefficients correspond to polynomials that are orthogonal with respect to the DCS that is used as a weight function. After applying the Golub and Welsch algorithm to these recurrence coefficients, the corresponding points and weights will satisfy eq. 3.10 for $l = 0, \dots, 2N-1$. That is, the first $2N$ moments of the DCS are preserved. However, as discussed,

the goal is to specifically avoid preservation of the zeroth moment, because the zeroth moment gives the total cross section or the MFP causing computational inefficiency. This is the motivation for using the Radau method discussed above. By requiring one discrete point is equal to unity, we generate a deflection cosine that corresponds to a non-interaction ($\zeta_{N+1} = 1 = \cos(0)$). A scattering angle of zero is equivalent to not interacting. Since the analog DCS is peaked about non-interaction, we seek to remove this feature from the GBFP DCSs. After generating the discrete points and weights only the points not equal to unity are kept.

To make this discussion clear, we will provide an example of the process of constructing a GBFP elastic scattering DCS. First, we must select a few parameters. We will demonstrate the process of generating 4 discrete points and weights for a 1 MeV electron in Gold with the following parameters:

- $Z=79$
- $A=196.97$ g/mol
- $\rho=19.33$ g/cc
- $\eta=1e-4$
- $N=4$

To generate polynomials that are orthogonal to the screened Rutherford DCS we need $2N+2$ moments given by

$$M_l = 2\pi \int_{-1}^1 P_l(\mu) \Sigma_n(E, \mu) d\mu. \quad (3.11)$$

There are several methods that can be used to generate these moments accurately. One is the Spencer recurrence [10]. This recurrence is only good for the screened Rutherford DCS over the full range. We implemented a more general method such that any elastic scattering DCS for the full or partial range is possible. This method simply uses adaptive quadrature to evaluate the integral in eq. 3.11 and gives the following for the first 10 moments:

Table 1: Moments of the Screened RutherfordAnalog DCS

l	M_l (1/cm)	l	M_l (1/cm)
0	13222.95284269771	5	12993.68379391062
1	13200.72491556212	6	12920.77698622844
2	13164.40260046155	7	12841.46869195591
3	13116.67842732473	8	12756.48220266539
4	13059.33200551864	9	12666.43977610700

We must now generate the first $2N+1$ recurrence coefficients for monic Legendre polynomials. The coefficients are given by

$$\begin{aligned}\alpha_j &= 0 \\ \beta_j &= \frac{1}{4 - \frac{1}{j^2}},\end{aligned}\tag{3.12}$$

where β_0 is not used and can be set to an arbitrary value. Given M_p , α_j , and β_j we can now generate the non-classical recurrence coefficients a_j and b_j . The result is

Table 2: Non-classical Recurrence Coefficients for Example Problem

j	a_j	b_j
0	0.9983189891546911	arbitrary
1	-0.004950428124079198	0.0004072459551613386
2	-0.002528000016159826	0.3308498723933296
3	-0.001661056221544444	0.2655511190282964
4	-0.001207307704623406	0.2564056575870433

The coefficients in table 2 are passed to the Radau algorithm and the discrete points and weights are generated. In table 3 and table 4, the discrete points and weights are given before and after regularizing or canceling the non-interaction point respectively.

Table 3: Example Discrete Cross-Section Before Regularizing

i	ζ_n	$\alpha(E)_n$
1	-0.8253336745219344	0.3542588039339951
2	-0.1926588357286153	1.46098457679131
3	0.5530858576077967	8.8112540880515
4	0.974594146260808	625.8776637056218
5	0.9999999999999994	12586.44868152331

Table 4: Example Discrete Cross-Section After Regularizing

i	ζ_n	$\alpha(E)_n$
1	-0.8253336745219344	0.3542588039339951
2	-0.1926588357286153	1.46098457679131
3	0.5530858576077967	8.8112540880515
4	0.974594146260808	625.8776637056218

The definition of the total cross section is the sum of the weights or 13222.9528 (1/cm) prior to regularizing. After regularizing, the total cross section is 636.5042 (1/cm). This means that the MFP associated with the regularized cross section is about 21 times longer than the analog MFP or on average a 1 MeV analog electron in gold suffers 21 times more collisions than a GBFP electron.

So far, we have discussed the elastic scattering DCS construction using quadrature methods. However, these methods are only valid over $[-1,1]$. Therefore, construction of a GBFP inelastic scattering DCS requires additional steps. It is possible to determine a linear mapping between Q , the dependent variable for inelastic scattering, and μ , the dependent variable for elastic scattering. That is, the following is true for the elastic and inelastic scattering DCSs:

$$\Sigma_e(E, Q) dQ = 2\pi \Sigma_n(E, \mu) d\mu. \quad (3.13)$$

Given a mapping, one can compute Legendre moments of the mapped inelastic scattering DCS. These moments are then used to generate points and weights on $[-1,1]$ and then the points and weights are mapped back to Q space. This process is outlined below.

First, we must determine a mapping. If we assume

$$Q(\mu) = m(1 - \mu) + b \quad (3.14)$$

and require that $Q(\mu=1) = Q_{\max}$ and $Q(\mu=-1) = 0$, we determine m and b such that

$$Q(\mu) = \frac{Q_{\max}}{2} (1 - \mu). \quad (3.15)$$

Given this mapping, we can now obtain a relationship between energy-loss moments, Q_n , and Legendre moments of a pseudo elastic scattering DCS or M_l . We would like to rewrite the right hand side of the following equation in terms of energy loss moments

$$M_l = 2\pi \int_{-1}^1 P_l(\mu) \Sigma_n(E, \mu) d\mu. \quad (3.16)$$

From our mapping, we know that $(1 - \mu) = \frac{2}{Q_{\max}} Q$ and we can rewrite $P_l(\mu)$ as

$$P_l(\mu) = \sum_{n=1}^l c_n^l \frac{(-1)^n}{n!} (1 - \mu)^n, \quad (3.17)$$

where

$$c_n^l = \frac{1}{2^n n!} \prod_{i=0}^{n-1} [l(l-1) - i(i-1)]. \quad (3.18)$$

Equation 3.16 becomes

$$M_l = 2\pi \sum_{j=1}^l c_j^l \frac{(-1)^j}{j!} \int_{-1}^1 (1-\mu)^j \Sigma_n(E, \mu) d\mu. \quad (3.19)$$

Then we substitute the expression for $(1-\mu)$ and $\Sigma_n(E, \mu) d\mu$ and change the limits of integration, which gives

$$M_l = \sum_{j=1}^l c_j^l \frac{(-1)^j}{j!} \left(\frac{2}{Q_{\max}}\right)^j \int_{Q_{\min}}^{Q_{\max}} Q^j \Sigma_e(E, Q) dQ \quad (3.20)$$

or

$$M_l = \sum_{j=1}^l c_j^l \frac{(-1)^j}{j!} \left(\frac{2}{Q_{\max}}\right)^j Q_j, \quad (3.21)$$

where

$$Q_j = \int_{Q_{\min}}^{Q_{\max}} Q^j \Sigma_e(E, Q) dQ. \quad (3.22)$$

are the energy-loss moments of the inelastic DCS.

The procedure for generating a GBFP inelastic DCS is the same as for the elastic DCS except we start with energy-loss moments. After mapping the moments, we can use the same procedure outlined earlier in this section. This will result in points that are on $[-1, 1]$ and we simply map those points back to Q space using eq. 3.15 to complete the process.

3.3. GBFP HYBRID CROSS-SECTION GENERATION

Generation of the hybrid DCS requires the same procedure discussed above, but the interval over which the discrete points are generated is restricted to $[\mu_{cut}, 1]$ for elastic scattering and $[Q_{\min}, Q_{cut}]$ for inelastic scattering. The remaining interval, $[-1, \mu_{cut}]$ and $[Q_{cut}, Q_{\max}]$, is represented exactly by the respective analog DCS. The first parameter that must be determined is the cut value. The cut value is driven by the underlying principle of the hybrid DCS. That is, by representing the catastrophic collisions (those resulting in large-angle deflection and large energy loss) with the analog DCS, discrete artifacts are mitigated. Therefore, selection of the cut should relate to how much of the GBFP DCS is represented by the analog DCS. To do so, we select the cut such that total cross section corresponding to the smooth portion of the GBFP DCS, Σ_t^S , is some fraction of the analog total cross section or

$$\Sigma_t^S(E) = \frac{\Sigma_t(E)}{N}. \quad (3.23)$$

We then solve for the cut by evaluating $\Sigma_t^S(E)$ or, for screened Rutherford elastic scattering,

$$\int_{-1}^{\mu_{cut}} \frac{C(E)}{[1-\mu+2\eta(E)]^2} d\mu = \frac{\Sigma_t(E)}{N}. \quad (3.24)$$

This gives

$$\mu_{cut} = 1 + 2\eta - \frac{N2\eta(1+\eta)}{1+N\eta}. \quad (3.25)$$

If N is unity, then the hybrid DCS goes over to the analog DCS. If N is large, $\mu_{cut} \rightarrow -1$ and the hybrid DCS goes over to discrete DCS. The cut value can be used to control the speed and accuracy of the hybrid model and must be determined by the applicable analog DCS.

Given a cut value, the moments used to obtain discrete points and weights for elastic scattering become

$$M_l = \int_{\mu_{cut}}^1 P_l(\mu) \Sigma_n(E, \mu) d\mu \quad (3.26)$$

and for inelastic scattering

$$Q_j = \int_{Q_{min}}^{Q_{cut}} Q^j \Sigma_e(E, Q) dQ. \quad (3.27)$$

The procedure for generating elastic scattering DCSs must change to incorporate a mapping from $[\mu_{cut}, 1]$ to $[-1, 1]$ before utilizing the MCA. A process similar to what was required for inelastic scattering is applied. Rather than going through the derivation of the mapping, we will simply provide the result. First, the mapping for the moments is

$$\nu_l = \sum_{n=0}^l c_n^l \frac{(-1)^n}{n!} \left(\frac{2}{1-\mu_{cut}} \right)^n \sum_{k=0}^n b_k^n M_k, \quad (3.28)$$

where M_k is given in eq. 3.26, c_n^l is given in eq. 3.18, and b_k^n is

$$b_k^n = \int_{-1}^1 P_k(\mu) (1-\mu)^n d\mu = \frac{2k+1}{2} \sum_{m=0}^k c_m^k \frac{(-1)^m}{m!} \frac{2^{n+m+1}}{n+m+1}. \quad (3.29)$$

If $\mu^* \in [\mu_{cut}, 1]$ and $\mu \in [-1, 1]$, the linear mapping from μ^* to μ is

$$\mu(\mu^*) = \frac{\mu_{cut} - 1}{2}(1 - \mu^*) + 1. \quad (3.30)$$

The procedure for generating discrete inelastic scattering DCSs remains the same except that the mapping changes to

$$Q(\mu) = \frac{Q_{cut}}{2}(1 - \mu) \quad (3.31)$$

and the moments supplied to the MCA are mapped from the moments in eq. 3.27.

3.4. IMPLEMENTATION OF THE GBFP MODELS IN GEANT4 TEST CODE

Geant4 is a toolkit for the simulation of the passage of particles through matter. Its areas of application include high energy nuclear and accelerator physics, medical physics, and space physics [4]. In general, use of Geant4 entails developing an application with at least three mandatory user-defined classes that are inherited from the base classes named *G4VDetectorConstruction*, *G4VPhysicsList*, and, *G4VPrimaryGeneratorAction*. Creation of a *G4VDetectorConstruction* inheriting classes is used to set the problem geometry. In this inheriting class, the dimensions and material properties for the model are set. A *G4VPhysicsList* inheriting class is used to set the various physics processes that are applicable for the particles required by the simulation. In this inheriting class, the processes and the associated models are created and applied to the appropriate particles. Finally, creation of a *G4VPrimaryGeneratorAction* inheriting class is used to define the particle source. The position, energy, particle type, and direction are set in this class (distributions for each of these parameters can be used as well). It is at the level of processes and models where the details of the implementation of the GBFP method are of interest. A process and model was written for each GBFP DCS (Discrete and Hybrid) and for each interaction (elastic and inelastic). In addition, a GBFP DCS generation tool was written and used by the various models.

The physics processes determine when and how to apply the physics (at the beginning of the step, along the step, or at the end of a step). For example, all of the physics processes created for the test code are single event, so the processes are applied at the end of a step. Depending on the type of process (elastic or inelastic) the process samples an angular deflection or energy loss and then updates the state of the particle accordingly. The physics models are used to define how to sample the collision outcome and the total cross section for that particular interaction. In addition, the data or the GBFP DCSs are prepared in the physics models before the run begins. A GBFP DCS and total cross section is generated for each element in the model at the time the physics models are initialized. However, one could generate a GBFP DCS database rather than preparing the data at the time of the run.

The discrete GBFP models are contained in a single class. However, the hybrid GBFP model is a combination of a soft collision model and a hard collision model. The soft collision model corresponds to the discrete portion of the DCS and has the same structure as the discrete GBFP models. The hard collision model corresponds to the smooth portion of the DCS and has the same structure as the analog DCS models.

Each of the following GBFP physics model and process classes are currently implemented:

- *AnalogScreenedRutherfordElasticScatteringModel*
- *AnalogScreenedRutherfordElasticScatteringProcess*
- *AnalogMottElasticScatteringModel*
- *AnalogMottElasticScatteringProcess*
- *AnalogRutherfordInelasticScatteringModel*
- *AnalogRutherfordInelasticScatteringProcess*
- *AnalogMöllerInelasticScatteringModel*

- AnalogMöllerInelasticScatteringProcess
- DiscreteScreenedRutherfordElasticScatteringModel
- DiscreteScreenedRutherfordElasticScatteringProcess
- DiscreteMottElasticScatteringModel
- DiscreteMottElasticScatteringProcess
- DiscreteRutherfordInelasticScatteringModel
- DiscreteRutherfordInelasticScatteringProcess
- DiscreteMöllerInelasticScatteringModel
- DiscreteMöllerInelasticScatteringProcess
- HybridSoftScreenedRutherfordElasticScatteringModel
- HybridSoftScreenedRutherfordElasticScatteringProcess
- HybridSoftMottElasticScatteringModel
- HybridSoftMottElasticScatteringProcess
- HybridSoftRutherfordInelasticScatteringModel
- HybridSoftRutherfordInelasticScatteringProcess
- HybridSoftMöllerInelasticScatteringModel
- HybridSoftMöllerInelasticScatteringProcess
- HybridHardScreenedRutherfordElasticScatteringModel
- HybridHardScreenedRutherfordElasticScatteringProcess
- HybridHardMottElasticScatteringModel
- HybridHardMottElasticScatteringProcess
- HybridHardRutherfordInelasticScatteringModel
- HybridHardRutherfordInelasticScatteringProcess
- HybridHardMöllerInelasticScatteringModel
- HybridHardMöllerInelasticScatteringProcess

4. RESULTS AND DISCUSSION

The following sections present results obtained since the last reporting period. Namely, the more interesting results from the test suite are highlighted. Each of the following items are discussed in remaining subsections

- CEASE-like problem
- Angular deflection distributions,
- Energy-loss spectra,
- Dose-depth curves,
- Two-dimension dose deposition,
- Reflection and transmission fractions.

The first item, “CEASE-like problem”, is a demonstration of the GBFP method in one-dimension slabs with thicknesses on the order of the CEASE (compact environmental anomaly sensor) silicon detectors. In addition, a source with a power law energy distribution was tested on these problems, since power law spectra are encountered in the radiation belts.

The remaining items are results from an extensive test suite. The test suite was used to find programming errors and to characterize the performance of the GBFP method for various problem parameters (e.g. particle energy, material type, result type, and so on).

All of the problems in the test suite have an associated length. For finite medium problems, the associated length gives a measure of the thickness of the medium. The length tested is related to a condensed history step-size. The definition of the step-size used in this paper and in many condensed history codes is

$$S_i = \int_{E_{i-1}}^{E_i} (-dE/dx)^{-1} dE, \quad (4.1)$$

where E_i is the initial energy of the particle at the beginning of the step, $(-dE/dx)$ is the stopping power, and

$$E_{i-1} = 2^{-1/8} E_i \quad (4.2)$$

is the energy of the particle at the end of the step. Therefore, a step-length is the distance traveled while slowing down from E_i to E_{i-1} . This metric is used for presenting results because it provides a length scale that is consistent with condensed history. That is, the GBFP method must be effective at these lengths to be considered a viable alternative. Results were generated for slabs with thicknesses of one sub-step, one step, and 10 steps according to the schematic in fig. 1. However, the quantities of interest vary from angular distributions to energy spectra and dose deposition profiles.

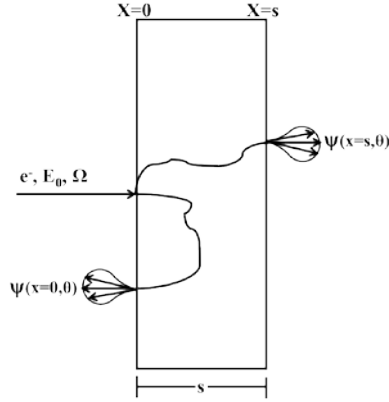


Figure 1: One-Dimension Slab Problem Schematic.

Since many of the following results were generated simultaneously, we report a single efficiency measure that provides a sense of the speed-ups achieved with the GBFP method. The following table gives the ratio of the wall time required for a GBFP simulation to the analog simulation. The tables indicate that there is a dependence on both the energy of the source particle and the level of accuracy of the approximation. For higher energy particles, the analog DCS is more peaked and the regularization process is much more significant. The resulting DCSs have longer MFPs for higher energy particles than for lower energy particles relative to the analog MFP. The other contributing factor impacting efficiency is the level of accuracy. The less accurate approximations are one to two orders of magnitude more efficient than the more accurate approximations. Ultimately, there is a clear trade-off between efficiency and accuracy. This poses an interesting optimization problem that will be addressed in future work. Regardless, it is clear that the GBFP method results in efficiency gains of one to two orders of magnitude over analog Monte Carlo.

Table 5: Ratio of Wall Time for Analog Simulation to Wall Time for GBFP Simulation.

Energy (keV)	Approximation			
	1 Angle, 1 Energy	2 Angles, 1 Energy	4 Angles, 1 Energy	8 Angles, 1 Energy
10	0	0	0	0
50	2	2	1	1
100	4	3	2	2
500	22	12	6	4
1000	40	21	10	6
5000	178	89	42	19
10000	381	196	90	41

Table 6: Ratio of Wall Time for Analog Simulation to Wall Time for GBFP Simulation Continued.

Energy (keV)	Approximation				
	Hybrid 1 Angle $\Sigma_t^s = \Sigma_t/_{10}$ 1 Energy	Hybrid 1 Angle $\Sigma_t^s = \Sigma_t/_{100}$ 1 Energy	Hybrid 1 Angle $\Sigma_t^s = \Sigma_t/_{1000}$ 1 Energy	1 Angle, Analog Energy	4 Angles Analog Energy
10	0	0	0	0	0
50	1	2	2	2	1
100	2	3	4	5	2
500	2	5	13	17	6
1000	2	6	17	26	9
5000	2	6	24	51	26
10000	2	6	25	60	38

4.1. CEASE-LIKE PROBLEM

Many of the results obtained from the test suite are for the most challenging problem in electron transport: a mono-energetic pencil beam incident on a thin slab. Pencil beams are difficult to resolve because they are localized in space, angle, and energy. Whereas, many sources encountered in real world problems are distributed in space, angle, and energy. The GBFP method is actually more accurate when simulating distributed sources. In addition, the GBFP method is more effective on thicker problems where the source particles suffer enough collisions to spread out in space, angle, and energy. We tested the GBFP method on slabs with thicknesses representative of the CEASE telescope silicon detectors (that is, 150 microns for dft and 500 microns for dbt seen in fig. 2 [11]). The CEASE is a small, lightweight, and low power, spacecraft instrument designed to measure the local space radiation environment and generate warnings of the space environment hazards of radiation damage, dielectric charging and single events effects [12]. The 150 micron slab is roughly 15 steps for a 100-keV electron.

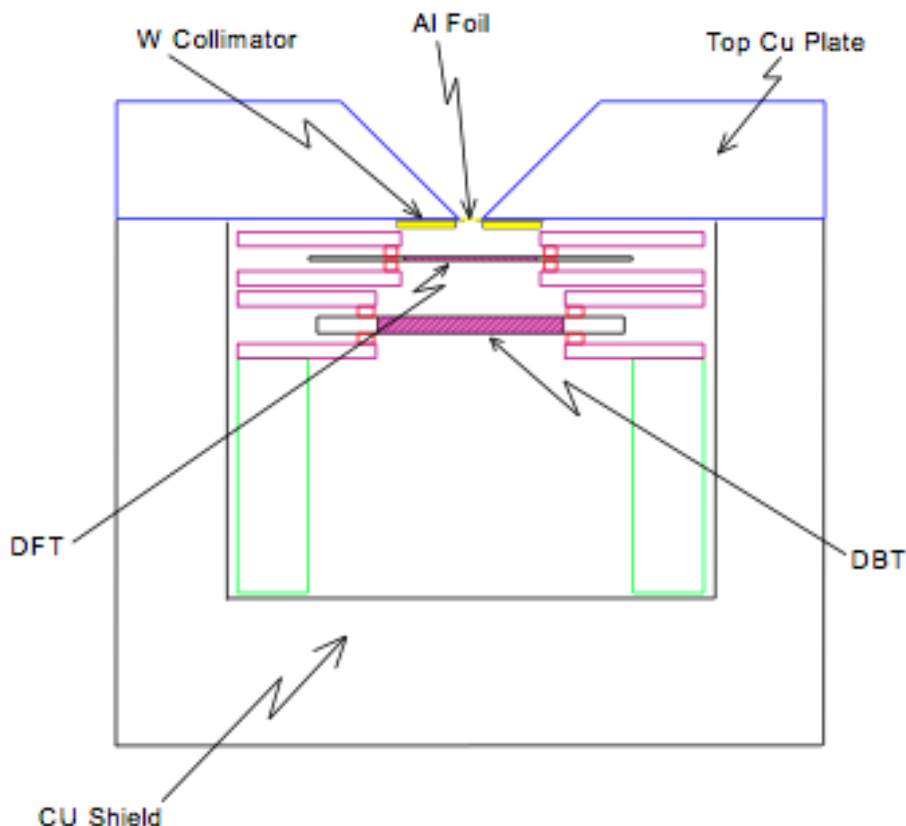


Figure 2: CEASE Particle Telescope Schematic.

We look at both energy spectrum and dose profiles since both of these quantities are relevant to response function generation. Response functions are necessary for interpreting raw satellite data, so it is important that the response functions are accurate. One method for determining response functions is simulating the response of a detector using a Monte Carlo particle transport code like Geant4 or MCNP. Assuming an extremely accurate geometric model of the detector is used, inaccuracies can only be a function of the physics employed. For this reason, it is important

for any approximation to properly capture quantities like energy spectrum and dose while remaining efficient. We will show that under these conditions, the GBFP method performs very well.

The following results were generated from simulations with a mono-directional, energy-dependent source. The source energy is sampled from a power law distribution, since a power law is representative of energy spectra encountered in the radiation belts. The source energies range from 1-keV to 10000-keV. The first result presented is transmitted energy spectrum in the 150-micron slab. As seen in the relative difference plot, each of the approximations are well within 5% of the benchmark.

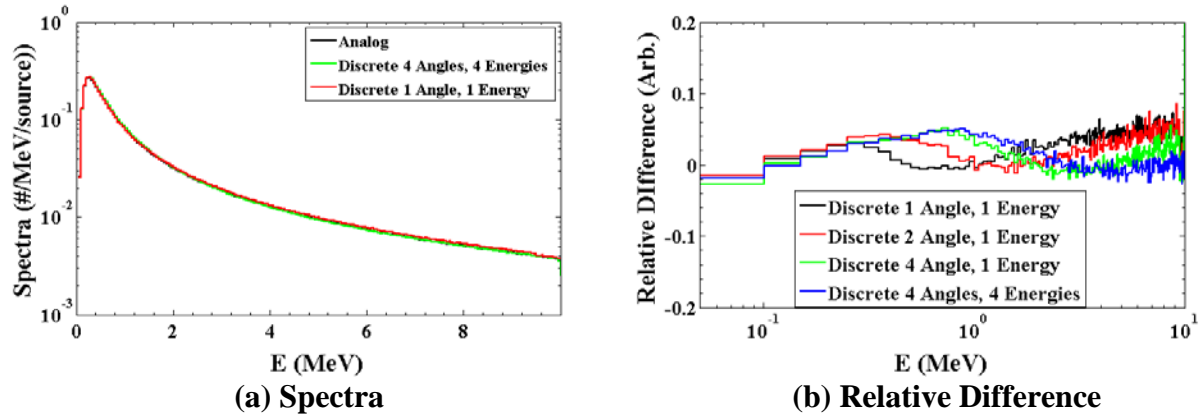


Figure 3: Reflected Energy Spectrum (a) and Relative Difference (b) for Electron Pencil Beam With Power Law Energy Distribution in 150 Microns of Silicon.

Next we present one-dimensional dose distributions. As seen in figs. 4a and 4b, and in 5a and 5b, each of the approximations are within a few percent of the benchmark.

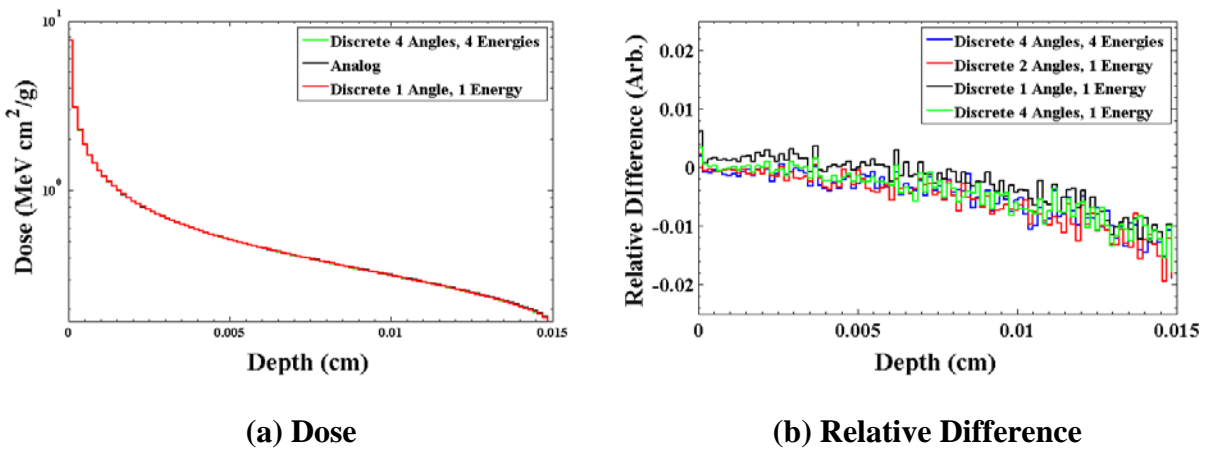
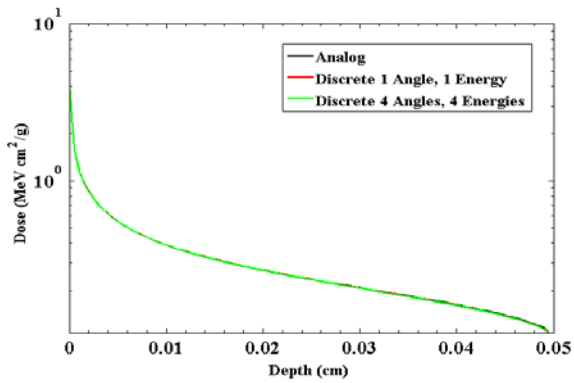
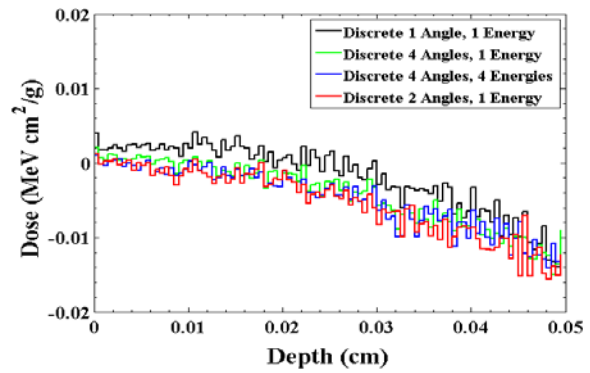


Figure 4: Dose (a) and Relative Difference (b) for Electron Pencil Beam With Power Law Energy Distribution in 150 Microns of Silicon.



(a) Dose



(b) Relative Difference

Figure 5: Dose (a) and Relative Difference (b) for Electron Pencil Beam With Power Law Energy Distribution in 500 Microns of Silicon.

The single-angle, single-energy approximation is very efficient at nearly 400 times more efficient than analog. Moreover, this approximation is within sufficient levels of accuracy making it a viable option for dose calculations or response function generation.

4.2. ANGULAR DEFLECTION DISTRIBUTIONS

In this section, we present the angular distributions of electrons that are either transmitted or reflected. Though test cases were completed for slabs with varying thicknesses, we focus our attention on the results for slabs with thicknesses of one step and discuss the impact of the thinner and thicker slabs. For these particular problem types, a mono-energetic electron source normally incident on the left face of a slab at $x = 0$ is simulated for source energies ranging from 100-keV to 10000-keV in low-Z, medium-Z, and high-Z materials (Silicon, Copper, Gold). However, we only present the GBFP method in low-Z materials because low-Z targets are the most challenging. Both elastic scattering and inelastic scattering are simulated using the screened Rutherford DCS and the Möller DCS respectively, along with GBFP approximations of these DCSs. The quantities of interest are the angular distributions of reflected and transmitted particles.

The benchmark solutions were obtained using the analog DCSs and are presented first to provide a sense of the physics. We begin with the transmitted angular distributions. In fig. 6, the transmitted angular distributions in silicon, copper, and gold for 100-keV and 10000-keV electrons and for a slab thickness of one step are presented. The two energies presented are the upper and lower energies that were tested and capture the impact of the source energy on the angular distribution. For lower energy particles, the screened Rutherford elastic scattering DCS is less peaked about forward scattering. In fact, for low enough energies the screened Rutherford elastic scattering DCS is nearly isotropic. Therefore, the resulting transmitted angular distributions are effectively isotropic. This is because isotropic scattering rapidly spreads out the mono-directional beam in angle. For higher energy particles, the screened Rutherford elastic scattering DCS is highly peaked and therefore spreading of the beam occurs slower. This is shown clearly in fig. 6 as the most peaked distributions correspond to the 10000-keV source and the more isotropic distributions correspond to the 100-keV source.

The anisotropy of the angular distributions depends on the peakedness of the DCS, but also on the number of collisions suffered by the particles. In thin slabs, most particles escape before suffering very many collisions and the resulting angular distributions are more peaked. In thick slabs particles suffer many more collisions and the initial beam is spread out in angle. However, the size of the slab is not the only mechanism that leads to a smoother angular distribution. For high-Z materials, the effect nuclear screening by the atomic electrons is stronger which leads to a larger average deflection cosine. That is, in high-Z materials, electrons scatter through larger angles on average than in low-Z materials causing additional spreading of the beam.

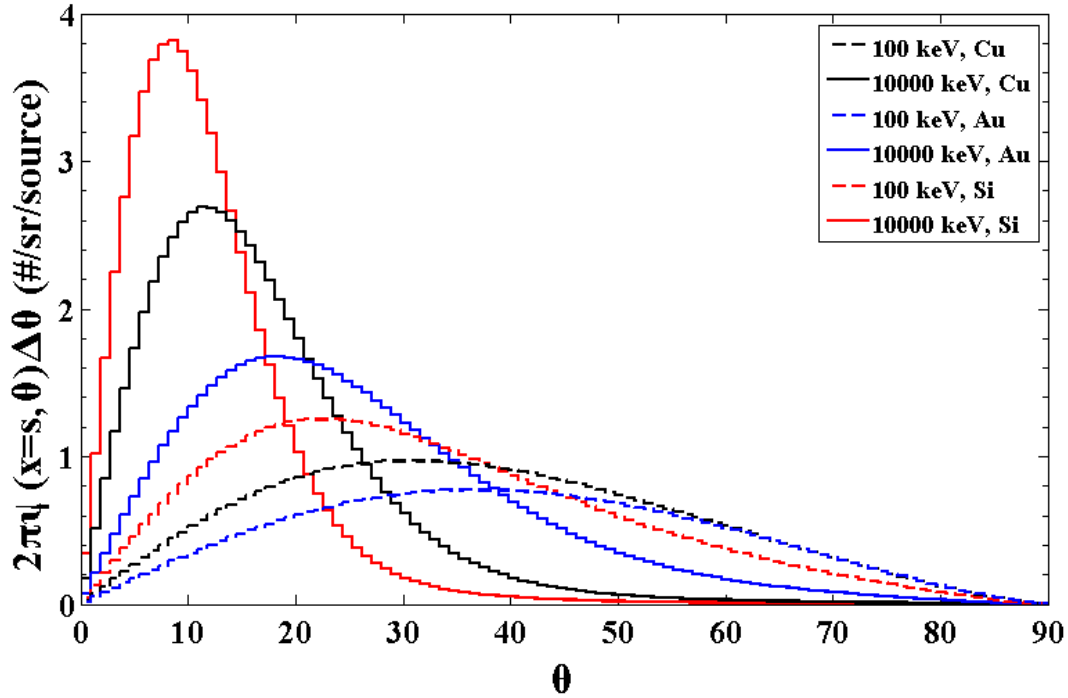


Figure 6: Transmitted Angular Distributions for 100-keV and 10000-keV Electrons in Silicon, Copper, and Gold Slabs with Thickness of One Step.

These benchmarks indicate that the peakedness of an angular distribution is strongly dependent on the source particles initial energy and also dependent on the atomic number of the target. It can be difficult to resolve the more peaked distributions with a discrete GBFP DCS. While this is true for GBFP DCSs with only a few points and weights, it is possible to resolve the transmitted and reflected angular distributions with a higher order GBFP DCS. In figs. 7a, 7b, 7c, and 7d transmitted angular distributions and relative differences for 100-keV electrons in silicon generated using the GBFP discrete and hybrid DCSs are compared with the benchmark. It is important to note that angular distributions are differential quantities, so they are difficult to resolve using any approximation; especially, for thin slab problems on the order of a stepsize in a low-Z material. That is, this is a very strict test of the GBFP method and for thicker slabs or higher-Z materials the GBFP method improves in accuracy.

The single-angle DCS results in severe discrete artifacts. Though a four-angle DCS dramatically improves the result, one must use eight points to completely smooth out the artifacts. The eight-angle DCS is within 5% of the analog solution. An alternative to adding more angles to remove artifacts is the hybrid DCS. The hybrid DCSs presented are represented by a single point for the peak and the remainder of the DCS represented by the smooth analog DCS. We only look at a few hybrid DCSs to show the effect of the cut value. The most efficient hybrid DCS, $\Sigma_t^s = \Sigma_t / 1000$, results in discrete artifacts. This is because the cut value is too far from unity and the discrete portion of the DCS dominates elastic scattering. By increasing the smooth total cross section by a factor of 10, or $\Sigma_t^s = \Sigma_t / 100$, the discrete artifacts are completely removed with exception of scattering angles that are roughly zero. We can refine the hybrid DCS further, where $\Sigma_t^s = \Sigma_t / 10$,

but there is only a subtle gain in accuracy for additional cost in efficiency. The impact of energy dependence is captured in the relative difference plot. For low energy particles, the addition of more discrete energies is almost negligible for the more accurate angular approximations. There is some smoothing of the discrete artifacts for the less accurate discrete angular approximations, but the artifacts remain. This indicates that a single-energy DCS may be sufficient when resolving angular distributions because the accuracy of the angular approximation is more important. The single-energy DCS preserves the first two moments, or stopping power and energy straggling, which seem to capture the majority of the energy-loss physics necessary for these cases.

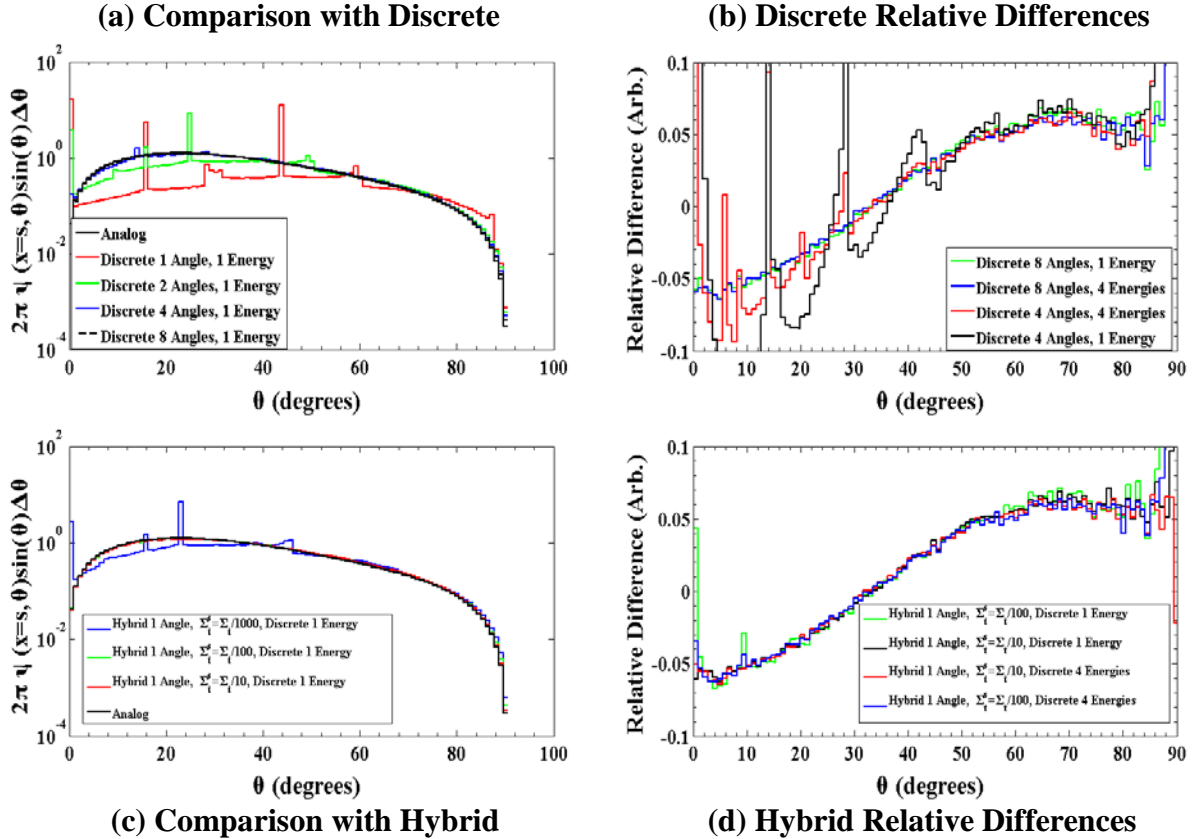


Figure 7: Comparison of GBFP and Benchmark Transmitted Angular Distributions using (a) Discrete and (c) Hybrid and the Relative Differences for (b) Discrete and (d) Hybrid for 100-keV Electrons in Silicon.

In figs. 8a, 8b, 8c, and 8d transmitted angular distributions for 10000-keV electrons in silicon generated using the GBFP discrete and hybrid DCS are compared with the benchmark. For higher energies, the impact of discrete artifacts is greater. Both a single-point and four-point DCS result in artifacts that overwhelm the angular distribution. At least an eight-point DCS is required to reduce the effects of the discrete artifacts. Some discrete artifacts are clear in the green curve for small scattering angles. However, even under this extreme test case, the addition of discrete energies smooth out these features. For the hybrid DCS the discrete artifacts are completely removed even with the most relaxed hybrid approximation.

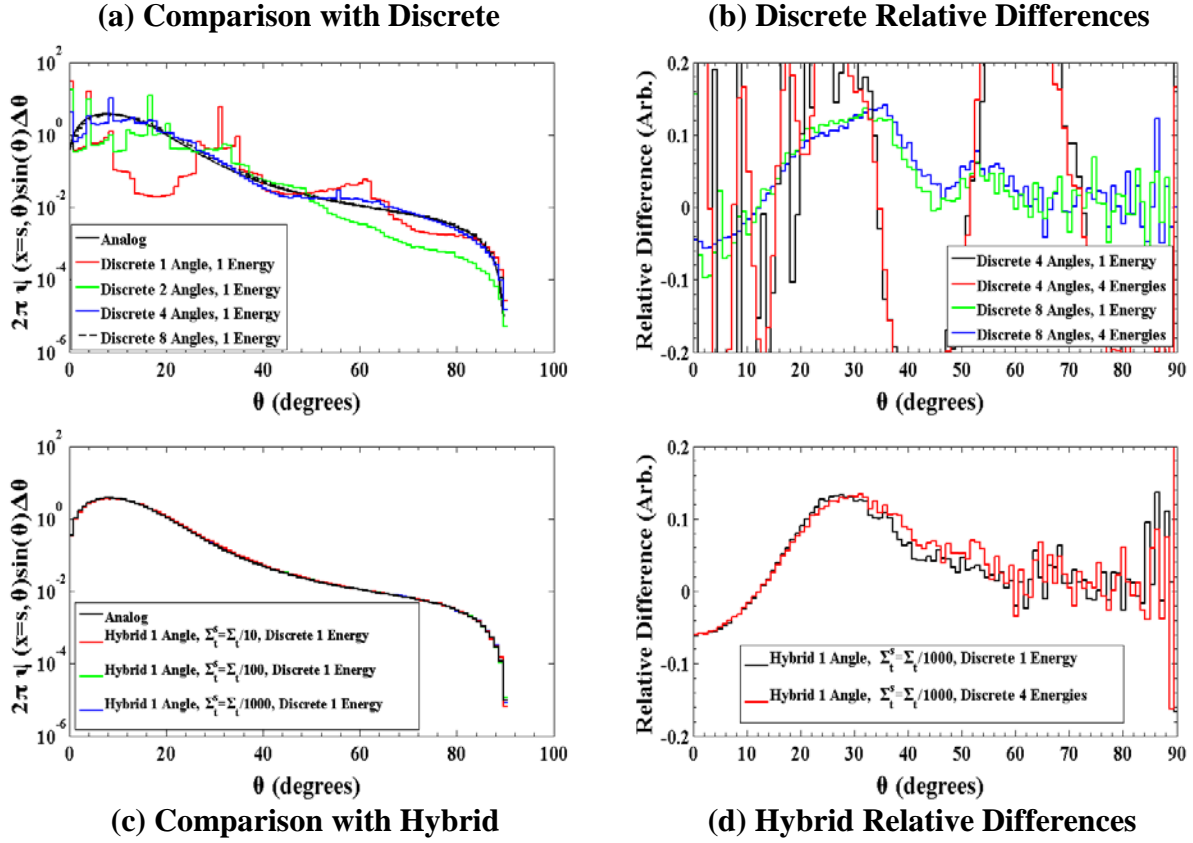


Figure 8: Comparison of GBFP and Benchmark Transmitted Angular Distributions using (a) Discrete and (c) Hybrid and the Relative Differences for (b) Discrete and (d) Hybrid for 10000-keV Electrons in Silicon.

Although the discrete DCS can result in discrete artifacts, these artifacts are not nearly as significant when calculating integral quantities like dose, charge deposition, or transmission and reflection (see following sections). If non-integral quantities like angular distributions are necessary, the hybrid DCS is effective at mitigating the discrete artifacts while still achieving some efficiency gains over analog.

In fig. 9, the reflected angular distributions in silicon, copper, and gold for various electron energies and for a slab thickness of one step are presented. This figure shows a result opposite of the transmitted angular distributions. That is, lower energy particles are more likely to be reflected so the magnitude of the lower energy curves is greater. However, there is a consistency between the transmitted and reflected angular distributions. In both results, the higher energy angular distributions are anisotropic (tend to be peak at 10-20 when transmitted degrees or 110-120 when reflected). However, the lower energy curves are nearly isotropic.

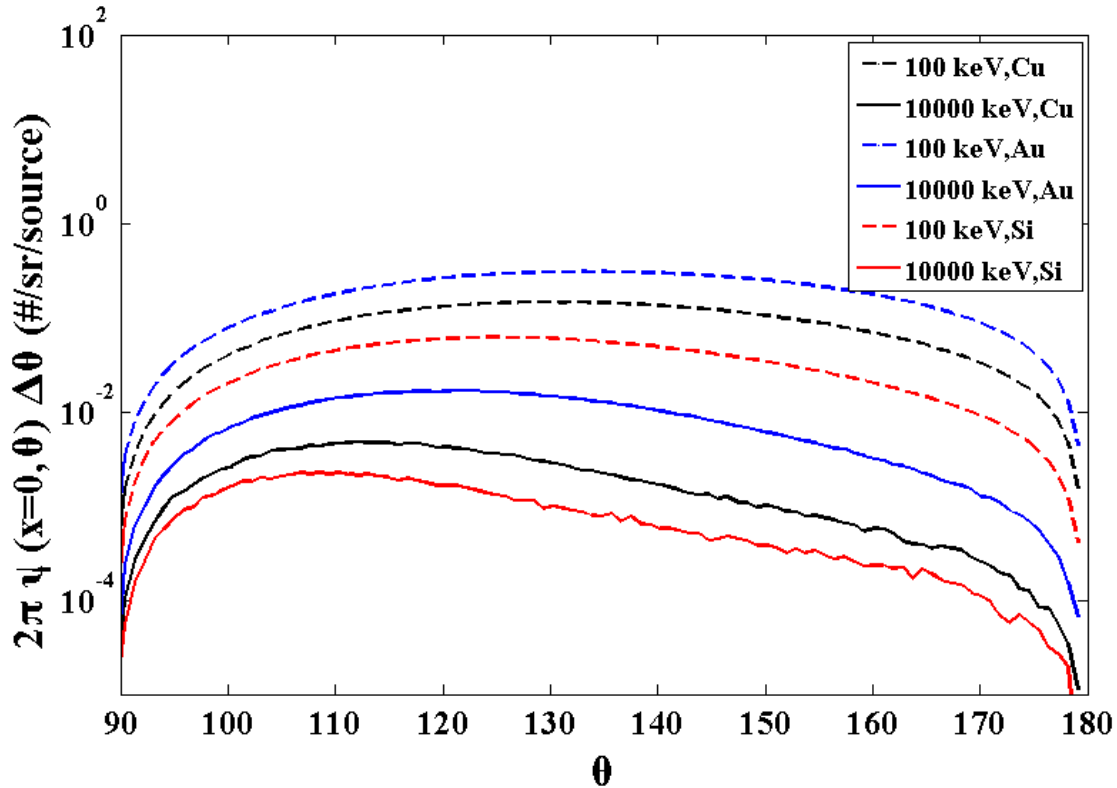


Figure 9: Reflected Angular Distributions for 100-keV and 10000-keV Electrons in Silicon, Copper, and Gold Slabs with a Thickness of One Step.

We now present results for the reflected angular distributions. In figs. 10a, 10b, 10c, and 10d reflected angular distributions for 100-keV electrons in silicon generated using the GBFP discrete and hybrid DCS are compared with the benchmark. Here, the discrete DCS results in artifacts for each of the DCSs tested. For 100-keV sources, a hybrid DCS with $\Sigma_t^s = \Sigma_t/1000$ is sufficient. It is likely that reflected particles typically result from hard collisions that are captured by the tail of the DCS or the smooth component. Therefore, any soft collisions that are captured by the single discrete angle do not contribute significantly to the solution and discrete artifacts are not present.

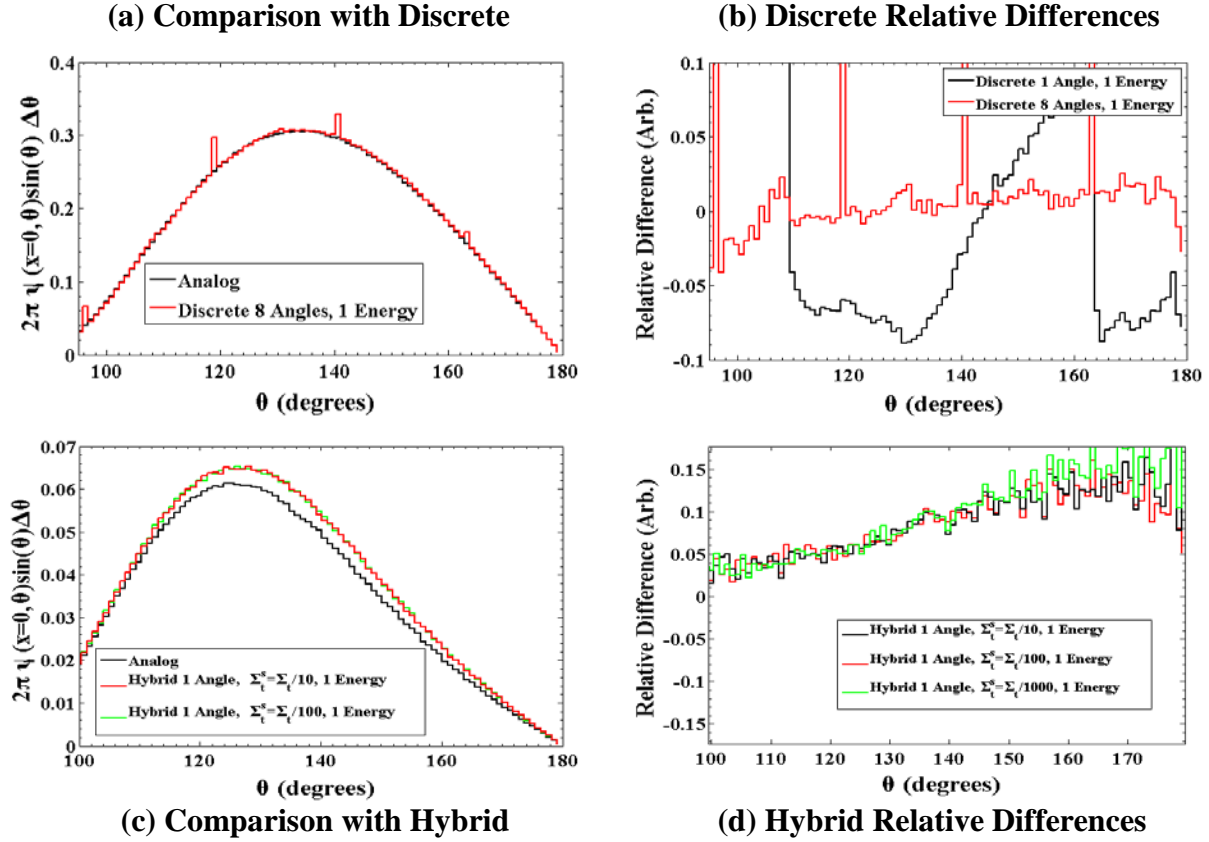


Figure 10: Comparison of GBFP and Benchmark Reflected Angular Distributions using (a) Discrete and (c) Hybrid and the Relative Differences for (b) Discrete and (d) Hybrid for 100-keV Electrons in Silicon.

In figs. 11a, 11b, 11c, and 11d, reflected angular distributions for 10000-keV electrons in silicon generated using GBFP discrete and hybrid DCSs are compared with the benchmark. Again, all of the discrete DCSs tested resulted in artifacts. For 10000-keV sources, a hybrid DCS with $\Sigma_t^s = \Sigma_t^s/1000$ is also sufficient. The higher energy results are statistically noisier than the low energy results because very few high-energy particles are reflected. However, these results still gives a sense of the resulting reflected angular distributions when using a hybrid DCS.

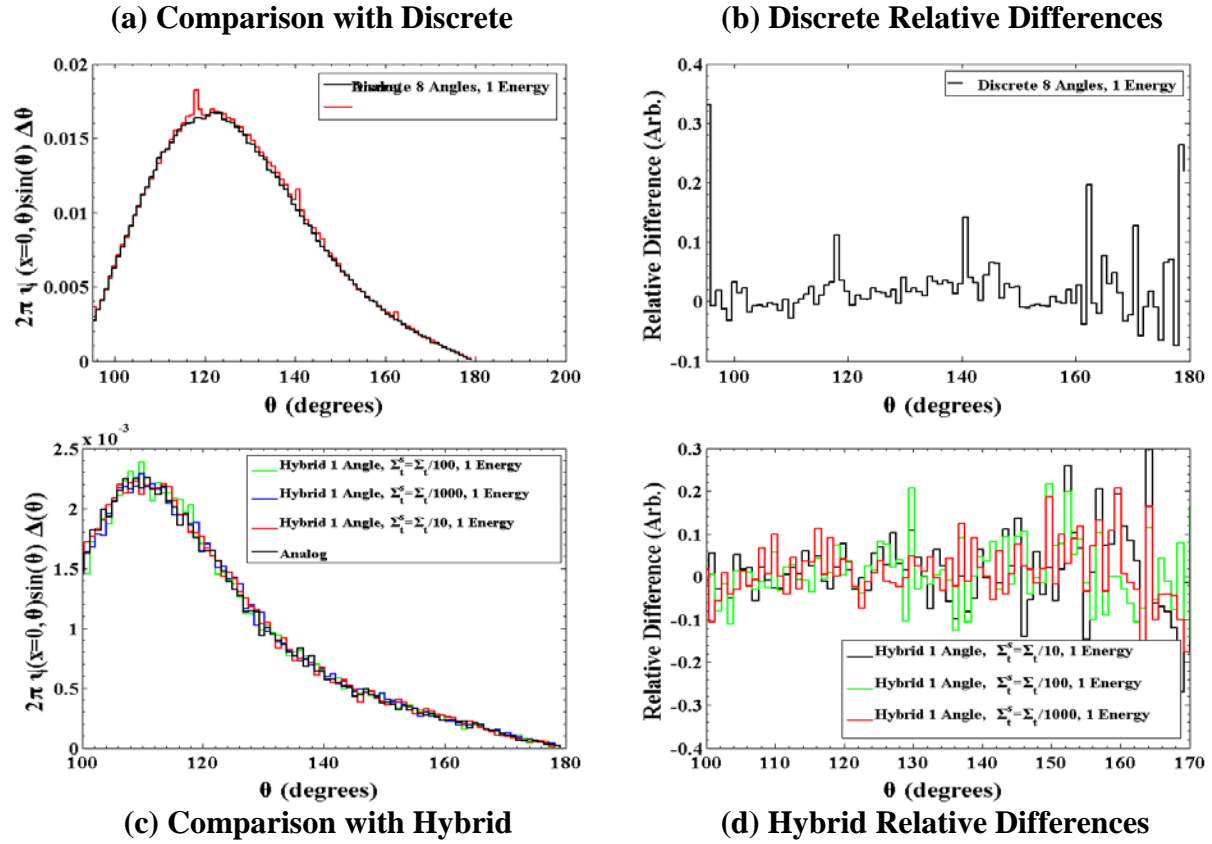
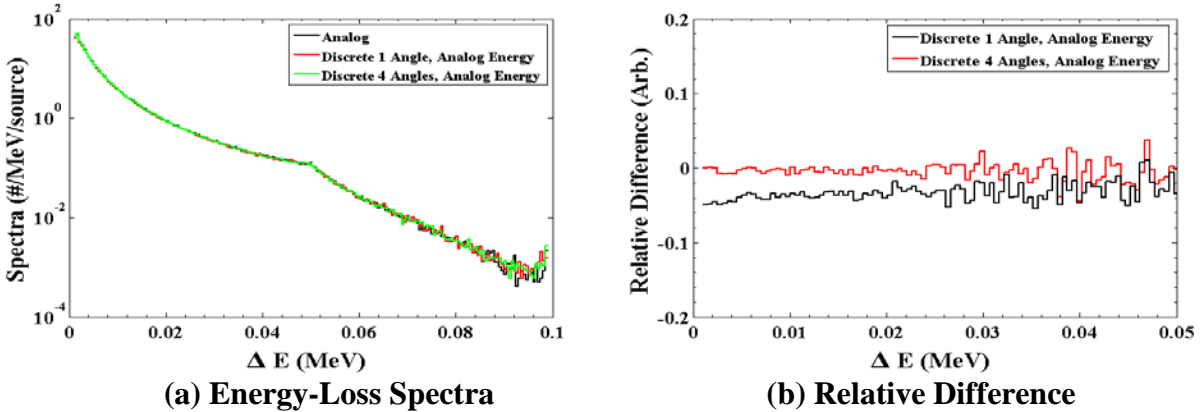


Figure 11: Comparison of GBFP and Benchmark Reflected Angular Distributions using (a) Discrete and (c) Hybrid and the Relative Differences for (b) Discrete and (d) Hybrid for 10000-keV Electrons in Silicon.

4.3.ENERGY-LOSS SPECTRA

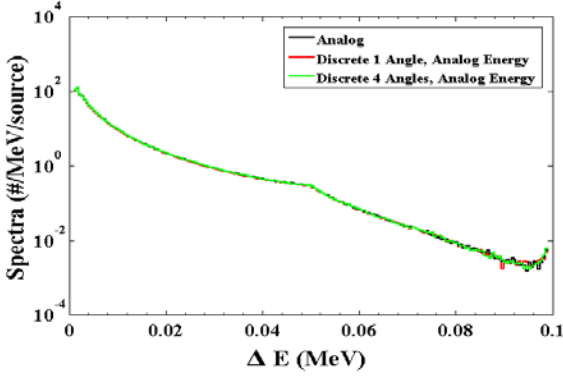
In this section, we present the energy-loss spectra for electrons that are either transmitted or reflected. The energy-loss spectra discussed below were obtained for thin slab problems according to the schematic in fig. 1 with exception that we are now interested in energy dependence rather than angular dependence. If a particle is transmitted or reflected the quantity tallied is the initial energy of the particle less the final energy of the particle or the total energy deposited in the slab by the particle.

We begin with the energy-loss spectra for 100-keV source particles. As a function of atomic number, the transmitted energy-loss spectra do not change significantly, so only gold results are presented. At lower energies, it may not be feasible to use a hybrid model because even with $\Sigma_t^s = \Sigma_t/5$ there is still significant disagreement for small energy transfers. If the smooth total cross section is pushed to roughly the analog total cross section, efficiency gains will be negligible. Therefore, a mixture of GBFP physics and analog physics were tested.

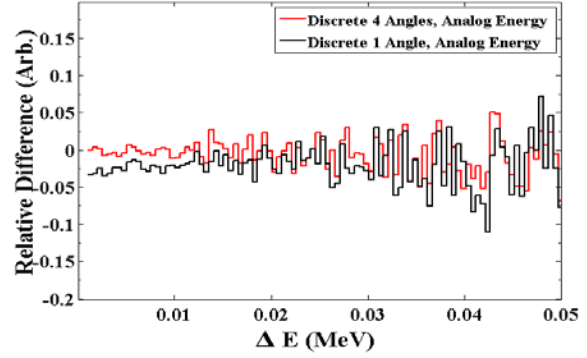


(a) Energy-Loss Spectra **(b) Relative Difference**
Figure 12: Reflected Energy-Loss Spectra (a) and Relative Difference (b) for 100-keV Electrons in Gold.

As seen in figs. 12a, 12b, 13a, and 13a, this approximation gives good agreement using only one discrete angle. The model using a single-angle DCS tends to underestimate the energy-loss spectra. Increasing the discrete elastic DCS to four angles results in very good agreement with the benchmark. One cause of this could be the relative size of the total cross section of elastic to inelastic scattering. That is, with a single-angle DCS, elastic scattering is no longer a dominant process. This results in more energy-loss collisions, so there are fewer particles transmitted because too many are deposited in the slab. Hence, the relative difference plots shows the spectrum is underestimated by about 5%. With the four-angle DCS, elastic scattering is better represented and the solution is improved greatly. In both cases, there are very few particles contributing beyond $Q > \frac{E_0}{2}$, so there are large oscillating relative differences for $Q > \frac{E_0}{2}$. Insufficient sampling rather than issues with the approximation causes the large oscillations. These results were not included in the relative difference plots.



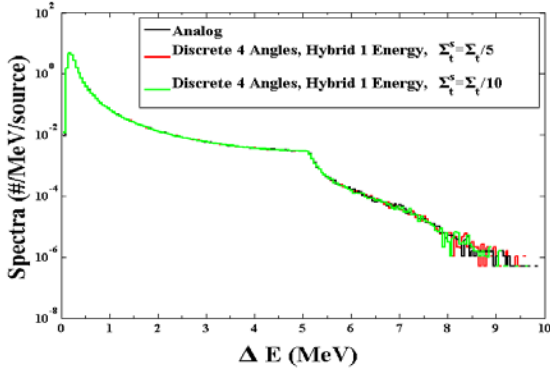
(a) Energy-Loss Spectra



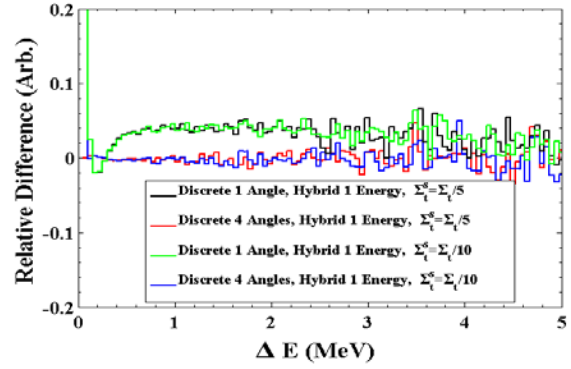
(b) Relative Difference

Figure 13: Transmitted Energy-Loss Spectra (a) and Relative Difference (b) for 100-keV Electrons in Gold.

For 10000-keV source electrons, results are given in figs. 14a and 14b. We only present the transmitted energy-loss spectra because the reflected energy-loss spectra were overwhelmed with statistical uncertainty. For higher energy electrons, the elastic DCS has a greater impact on accuracy. In this case, the single angle model is very close to unity, so a majority of the particles are pushed through the slab with small losses in energy. Hence, the small energy losses are overestimated for the single-angle approximations. Refining the angular model improves the estimation of the small energy losses. Additionally, hybrid models are effective at higher energies.



(a) Energy-Loss Spectra



(b) Relative Difference

Figure 14: Transmitted Energy-Loss Spectra (a) and Relative Difference (b) for 10000-keV Electrons in Gold.

4.4. DOSE-DEPTH CURVES

In this section, we present the dose-depth curves for electrons in gold. The dose-depth curves discussed below were obtained for thin slab problems according to the schematic in fig. 1 with exception that we are now interested in the spatial distribution of dose deposited throughout the slab. A key distinction between electrons and heavy charged particles is the Bragg peak or lack thereof. Since electrons more often undergo large-angle scattering, the Bragg peak is diffused out. Figures 15 and 16 present the dose-depth curves for 100-keV and 10000-keV electrons in gold.

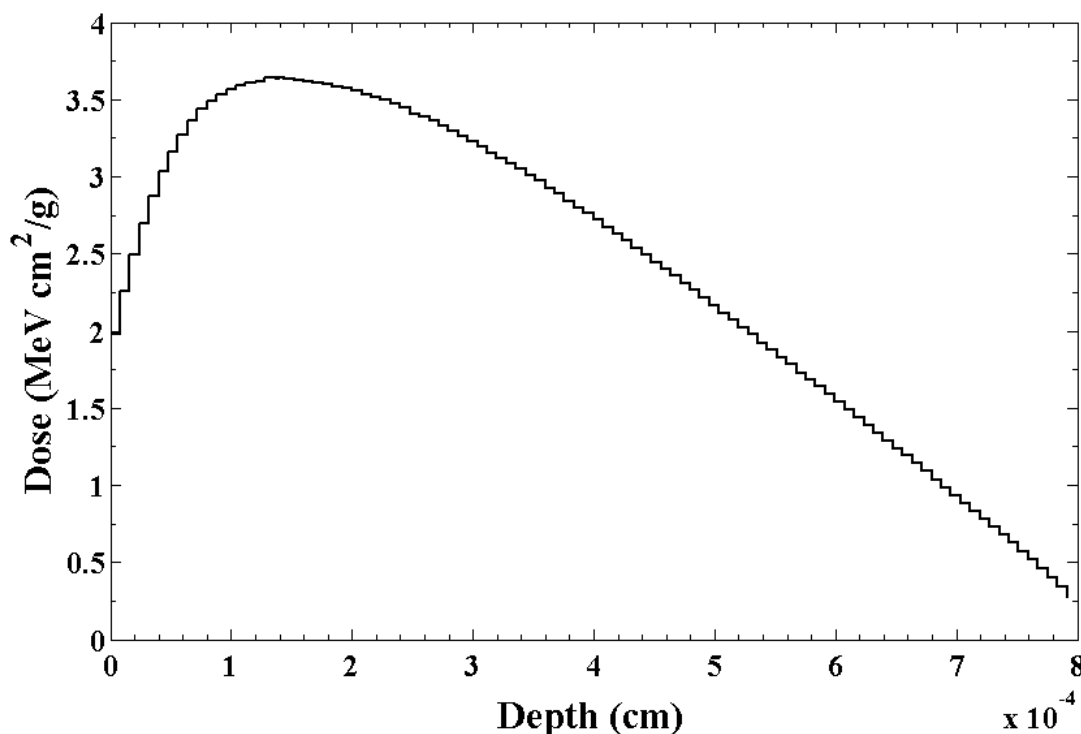


Figure 15: Analog Dose Profile for 100-keV Electrons in Gold Slab with a Thickness of One Step.

In figs. 15 and 16, there is no Bragg peak. The only major distinction between the low-energy and high-energy problems is that the peak of the distribution is pushed further into the slab because high-energy electrons are significantly more likely to scatter in forward directions.

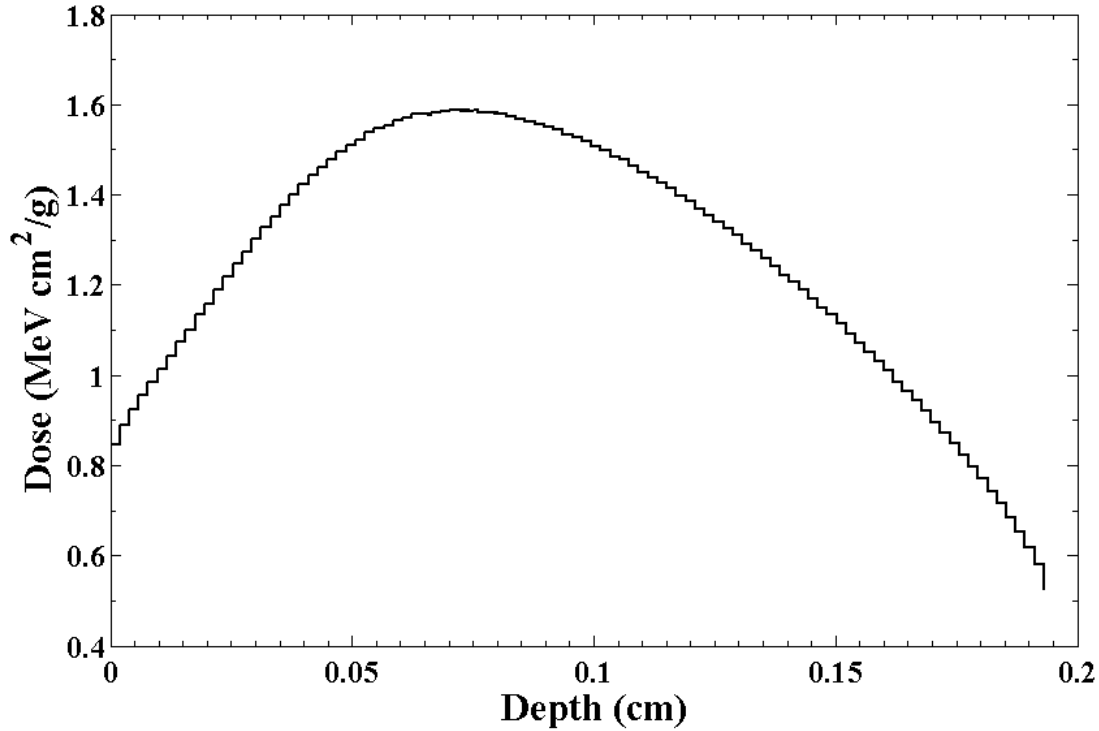
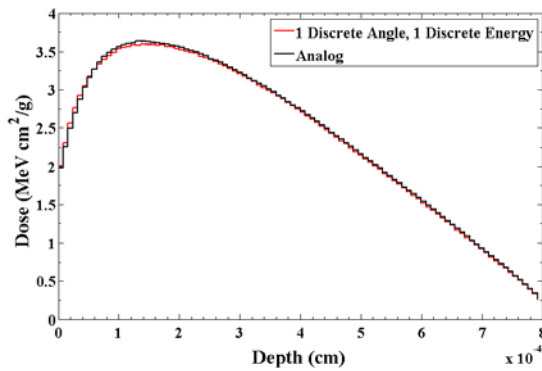
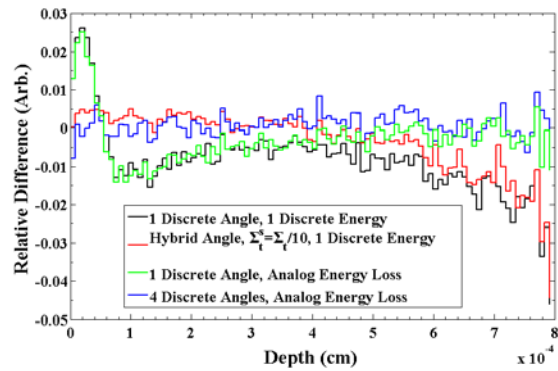


Figure 16: Analog Dose Profile for 10000-keV Electrons in Gold Slab with a Thickness of One Step.

In figs. 17a and 17b, comparisons of the approximations with the benchmark for 100-keV source electrons are presented. Results for four different approximations are shown to capture the effect of dependence on angle and energy. For both single-angle approximations, the dose is overestimated in the first few cells and then underestimated throughout the remaining cells. Regardless, both single-angle approximations are within roughly 3% of the analog solution. Further, improvement in accuracy (within 1% of analog) is achieved by using a hybrid elastic scattering DCS or a mixture of a four-angle discrete DCS with an analog inelastic scattering DCS. The latter being more efficient.



(a) Dose



(b) Relative Difference

Figure 17: Dose Profiles (a) and Relative Difference (b) for 100-keV Electrons in Gold.

In figs. 18a and 18b, comparisons of the approximations with the benchmark for 10000-keV source electrons are presented. Again, for both single-angle approximations, the dose is overestimated in the first few cells and then underestimated throughout the remaining cells. For the high-energy problem, the impact of inelastic scattering is slightly more significant. That is, it does not matter how accurate the elastic scattering DCS is if the inelastic scattering DCS is a single-energy point. In fact, the elastic scattering approximation can be relaxed to a four-angle DCS if an analog inelastic scattering DCS is used. From an efficiency standpoint, it is advantageous to use the four-angle discrete DCS with an analog inelastic scattering DCS rather than a hybrid angle, discrete energy approximation as it is 1.5-20 times more efficient depending on the hybrid DCS used.

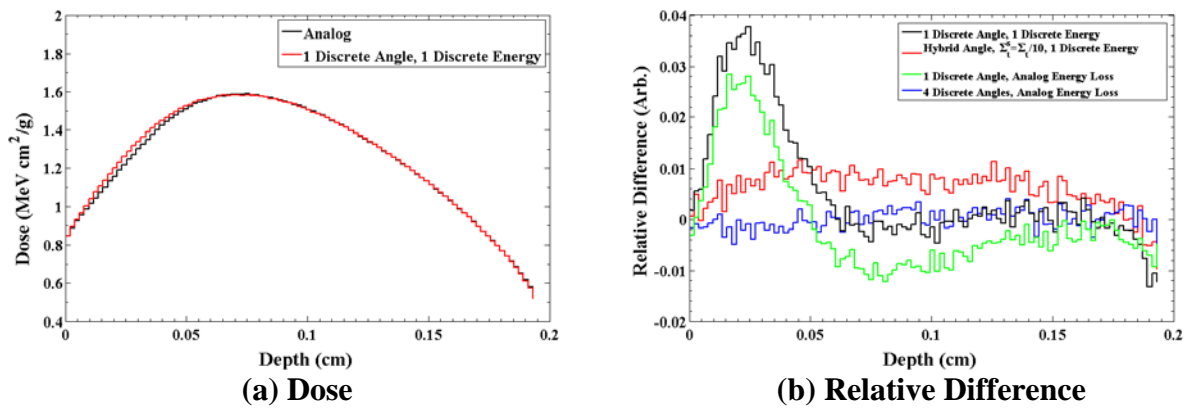


Figure 18: Dose Profiles (a) and Relative Difference (b) for 10000-keV Electrons in Gold.

4.5. TWO-DIMENSIONION DOSE DEPOSITION

In this section, two-dimension dose deposition results are presented. The problem setup is shown in fig. 19. For this simulation, 250-keV electrons are normal on a cube of silicon surrounding a small gold region. The electrons are normally incident on the bottom face of the cube and positioned at the interface of the two materials. There is a thin layer of silicon before the interface to ensure that the beam is spread slightly before reaching the interface. The dose is averaged over the x-dimension.

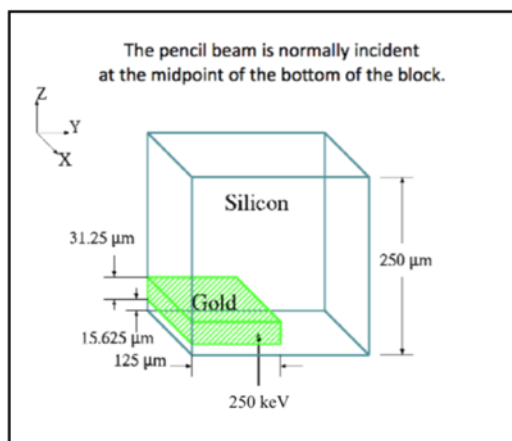


Figure 19: Two-Dimension Dose Deposition Problem Schematic.

The purpose of simulating this problem was to demonstrate the boundary crossing issues inherent to condensed history methods. 20 presents the analog benchmark. The actual structure of the gold region imbedded in the silicon shows up in the figure. Upon entering the gold region, electrons lose energy rapidly. Some electrons are reflected out of the gold and others never enter the gold region. These electrons that deposit energy in the silicon region do so at a slower rate and the benchmark shows a smoother gradient in the dose in the silicon region.

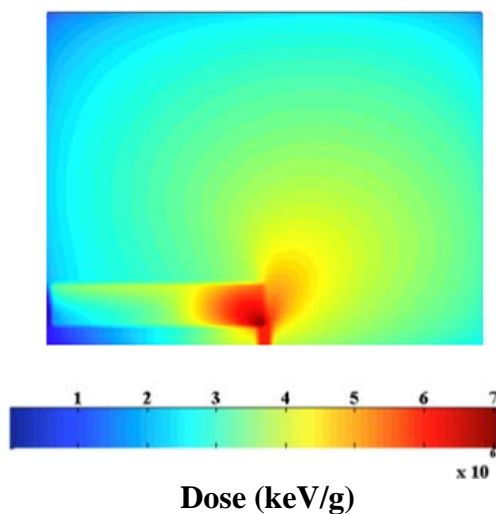


Figure 20: Dose Deposition Benchmark for 250-keV Electrons in Silicon Cube Gold with Insert.

In fig. 21, a comparison of the GBFP method and the Geant4 default physics with the benchmark is presented. The two left plots are the two most efficient approximations. The GBFP approximation shows some clear discrete artifacts that are not present in the one-dimension results. Since the single-angle GBFP approximation only allows forward scattering, most of the dose is pushed forward into the cube and does not spread significantly about the beam-line. However, the single-angle GBFP approximation does provide better results at the interface than the Geant4 default physics.

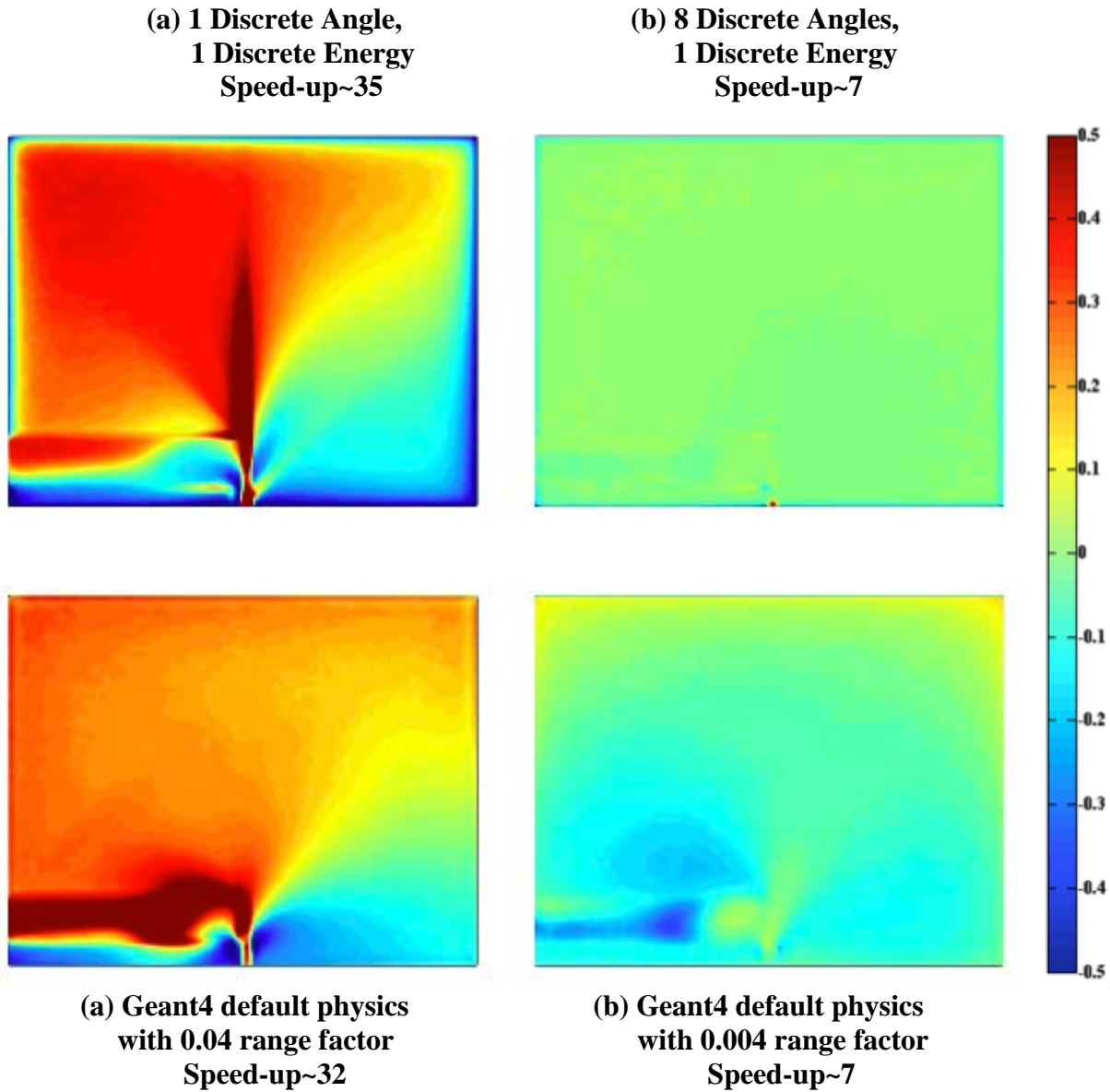


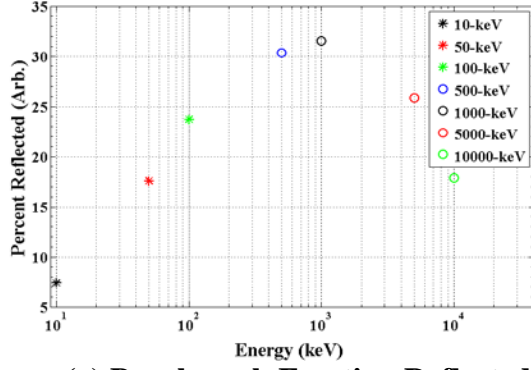
Figure 21: Dose Deposition for 250-keV Electrons in Silicon Cube With Gold Insert Using (A) GBFP 1 Discrete Angle, 1 Discrete Energy, (b) Geant4 Default Physics with 0.04 range Factor, (c) GBFP 8 Discrete Angles, 1 Discrete Energy, and (d) Geant4 Default Physics with 0.004 range factor.

The improved GBFP approximation is significantly more accurate and only disagrees with the benchmark very close to the source. Again, the comparable Geant4 default physics model is less accurate than the GBFP method especially near the interface.

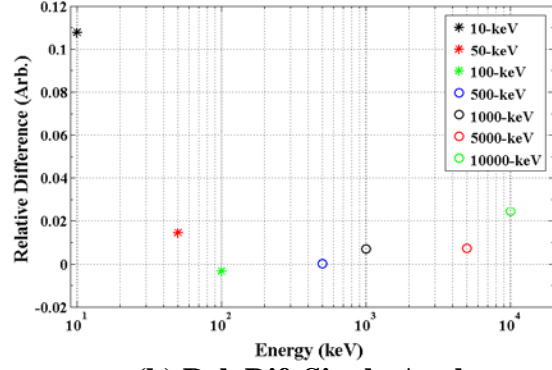
4.6. REFLECTION AND TRANSMISSION FRACTIONS

In this section, we present the reflection and transmission fractions. The reflection and transmission fractions discussed below were obtained for thin slab problems according to the schematic in fig. 1 with exception that we are now interested in the fraction of particles transmitted or reflected. For these calculations, electrons with energies below 5-keV are assumed to deposit all energy locally. This assumption leads to low reflection results for low energy electrons. Though this doesn't model reality, this assumption was consistent between the benchmark and the approximations.

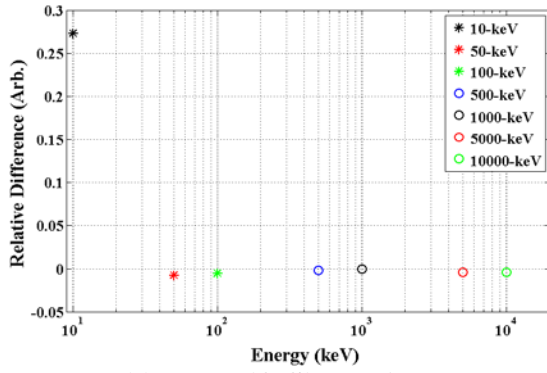
In figs. 22a, 22b, 22c, and 22d, the percent of particles reflected for the benchmark and the relative differences for three approximations are presented. The single-angle, single-energy approximation is within roughly 2% agreement with the benchmark except for 10-keV source particles. For 10-keV particles, the single-angle is nearly 90° , so after only two collisions the particle could be reflected. As the source energy gets higher, 50-keV, the single angles are already significantly more forward peaked, so they must suffer several collisions before being reflected. With the mixed GBFP DCS and analog DCS approximations, the 10-keV simulation gets worse. Since the inelastic scattering is the dominant process as the analog inelastic MFP is simulated, particles likely undergo several inelastic collisions before experiencing an angular deflection. As the particles energy drops below 10-keV, the single-angle DCS is represented by an angle greater than 90° or a backscatter. After backscattering, the particle undergoes several more inelastic collisions and then escapes the slab. The fact that the approximation gets worse going from a single-energy inelastic DCS to an analog inelastic DCS, indicates that there is some cancellation of error in the fully discrete approximation at 10-keV. The most accurate approximation uses four angles and has very good agreement with the benchmark.



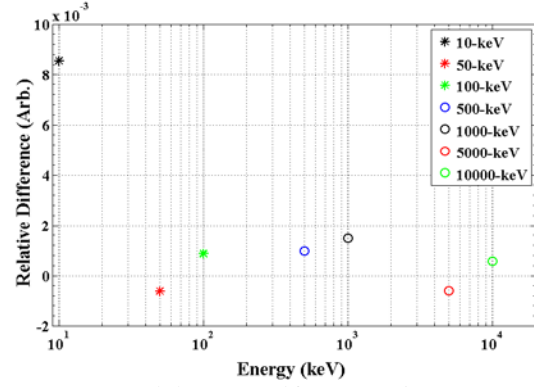
(a) Benchmark Fraction Reflected



(b) Rel. Dif. Single-Angle, Single-Energy DCS



(c) Rel. Dif. Single-Angle, Analog Inelastic DCS



(d) Rel. Dif. Four-Angle, Analog Inelastic DCS

Figure 22: The Fraction of Particles Reflected (a) and the relative difference for (b) Single-Angle, Single-Energy DCS, (c) Single-Angle, Analog Inelastic DCS, and (d) Four-Angle, Analog Inelastic DCS.

In figs. 23a, 23b, 23c, and 23d the percent of particles transmitted for the benchmark and the relative differences for three approximations are presented. The single-angle, single-energy approximation is within roughly 1-4% agreement with the benchmark. The mixed GBFP DCS and analog DCS approximations are an improvement over the fully discrete approximation. Again, the most accurate four-angle approximation has very good agreement with the benchmark.

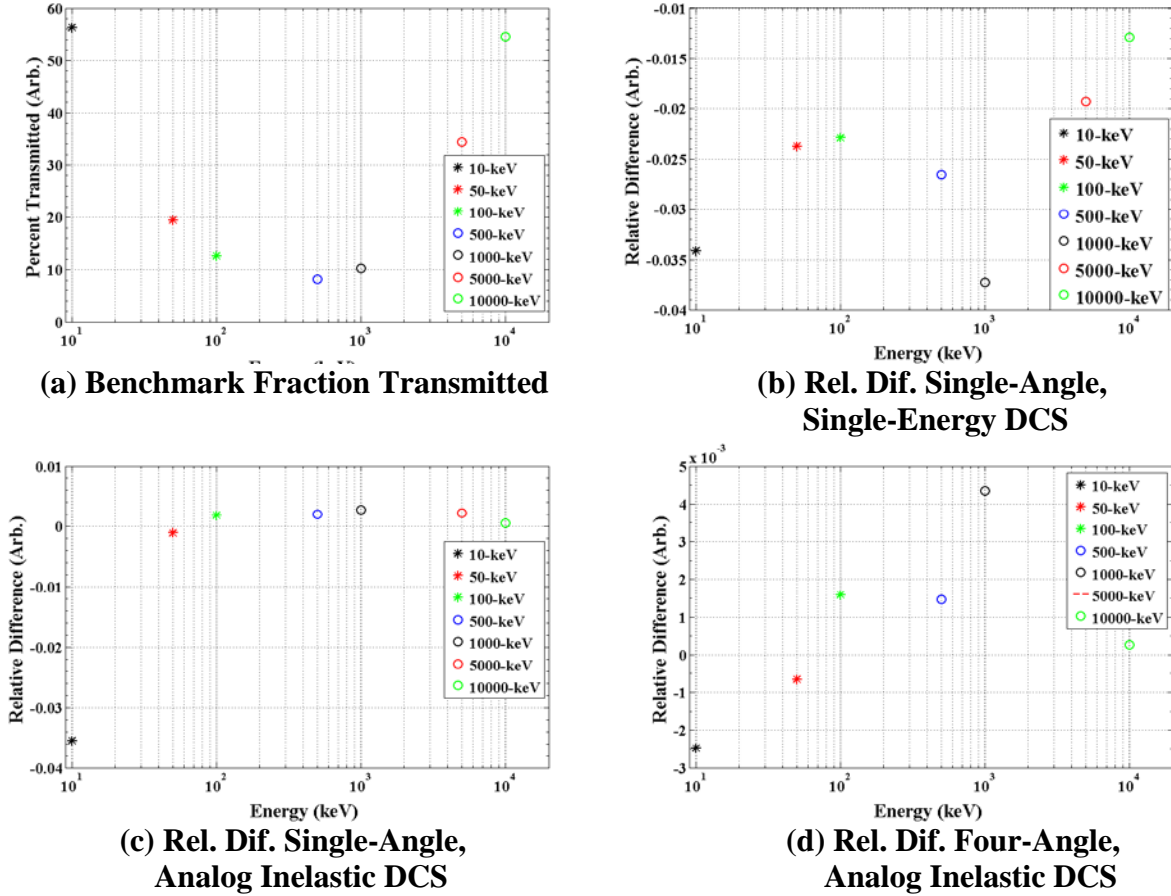


Figure 23: The Fraction of Particles Transmitted (a) and the relative difference for (b) Single-Angle, Single-Energy DCS, (c) Single-Angle, Analog Inelastic DCS, and (d) Four-Angle, Analog Inelastic DCS.

5. CONCLUSIONS

In many of the test cases, the GBFP method demonstrated superb efficiency gains over analog with acceptable levels of accuracy. In comparison with the Geant4 default physics, the GBFP method tended to give more accurate results for the same efficiency cost. Extensive testing was completed and valuable information for improvement of the current implementation was gained from the test suite. Corrections were made to the test code to account for the programming errors encountered during the extensive testing. Though the findings from initial test suite were promising, several test cases remain. Additional multilayer problems should be completed to better understand the accuracy of the GBFP method at boundaries. In addition, only normal incident sources were thoroughly tested, so several off-normal beam sources should be studied to see how angle of incidence impacts particle reflection. Also, the partial-wave DCSs were not thoroughly studied. Thorough testing of the DCS data will provide an interesting insight into the physics and more practical details like data storage issues.

Implementation of the advance Monte Carlo method for charged particles, the GBFP method, is nearly complete. Once secondary electron production is incorporated, implementation of the physics will be complete. Additional testing will begin to determine the accuracy of the GBFP method when calculating quantities more relevant to secondaries like charge deposition. Currently, the ability of GBFP to handle secondaries is unknown, but presumed to be problematic. Since the GBFP inherently does not preserve the total cross section, and, therefore, particle number, it is possible that only a mixture of GBFP elastic scattering and analog inelastic scattering will result in accurate and efficient charged deposition results.

There is still an additional implementation detail that must be addressed. That is, adaptive GBFP physics. Adaptive GBFP physics will provide users with an on-the-fly optimization of efficiency and accuracy for various applications. The purpose of adaptivity is to relieve users from the need to determine an optimal GBFP representation of the physics for their problem by trial and error. We saw that for dose calculations, the first few cells closest to the source require a more accurate representation of the DCSs. However, as the beam spreads further into the slab, the DCS can be relaxed into a more efficient representation and still maintain sufficient levels of accuracy.

REFERENCES

- [1] Lorence, L. J., Morel, J. E., Valdez, G. D., Physics Guide to CEPXS: A Multigroup Coupled Electron-Photon Cross Section Generation Code, SAND89-1685, Sandia National Laboratories, 1989.
- [2] Salvat, F., Jablonski, A., and Powel, C. J., ELSEPA – Partial-Wave Calculation of Elastic Scattering of Electrons and Positrons by Atoms, Positive Ions and Molecules, Computer Physics Communications, 165, pp. 157-190, 2005.
- [3] Evans, R. D., The Atomic Nucleus, 2nd Ed., McGraw Hill, 1955.
- [4] Geant4 CERN, Accessed May 6, 2013, <http://geant4.cern.ch>, 2012.
- [5] Geant4 Collaboration, Physics Reference Manual, Geant4.9.6, 2012.
- [6] Lewis, H. W., Multiple Scattering in an Infinite Medium, Physical Review, Volume 78, Number 5, June 1, 1950.
- [7] Gautschi, W., Questions of Numerical Condition Related to Polynomials, Studies in Numerical Analysis, MAA Studies in Math, 24, 1984.
- [8] Golub, G. H., Calculation of Gauss Quadrature Rules, Mathematics of Computation, Volume 23, Number 106, April 1969.
- [9] Golub, G. H., Some Modified Matrix Eigenvalue Problems, Society for Industrial and Applied Mathematics, Volume 15, Number 2, April 1973.
- [10] Spencer, L. V., Theory of Electron Penetration, Phys. Rev., 98, pp. 1597-1615, 1955.
- [11] Dichter, B. K., et al., Space Particle Modeling, Measurements, and Effects: Compact Environmental Anomaly Sensor (CEASE) Proton Calibration, AFRL-RV-HA-TR-2010-1117, Assurance Technology Corp., Carlisle, MA, 7 February 2011.
- [12] Dichter, B. K., et al., Compact Environmental Anomaly Sensor (CEASE): A Novel Spacecraft Instrument for In Situ Measurements of Environmental Conditions, IEEE Trans. Nucl. Sci., 45, December 1998.

LIST OF SYMBOLS, ABBREVIATIONS, AND ACRONYMS

AFRL	Air Force Research Laboratory
DCS	Differential Cross Section
GBFP	Generalized Boltzmann Fokker-Plank
MFP	Mean Free Path
UNM	University of New Mexico

DISTRIBUTION LIST

DTIC/OCF	
8725 John J. Kingman Rd, Suite 0944	
Ft Belvoir, VA 22060-6218	1 cy
AFRL/RVIL	
Kirtland AFB, NM 87117-5776	2 cys
Official Record Copy	
AFRL/RVBXR/Adrian Wheelock	1 cy

This page is intentionally left blank.